

**TRACKING AND LOCATING EVOLVING SOURCES USING INFRASOUND
AT SANTIAGUITO VOLCANO, GUATEMALA**

By

Kyle Richard Jones

Submitted in Partial Fulfillment
of the Requirements for the Degree of
Master of Science in Geophysics (Solid Earth)

New Mexico Institute of Mining and Technology
Socorro, New Mexico

July 2009

To my parents who never stopped believing in me and have always encouraged me to
dream big and aim for the stars.

Kyle R Jones

July 2009

“Never for me the lowered banner, never the last endeavor.”

-Sir Ernest Shackleton

ABSTRACT

Distinct sub-events can be identified and located during long duration (>50 s) and short duration (<50 s) volcanic eruptions by utilizing time-domain cross-correlation data from a three-station infrasound network at Santiaguito Volcano, Guatemala. Cross-correlation between each station pair using two-second time windows overlapping by 1.6 s allows determination of accurate acoustic interstation phase delay-times. Phase delay-times are used to calculate and locate time-varying source locations over the duration of an eruption. The mapped Santiaguito acoustic sources are considered to be a superposition of spatially and temporally distinct explosions (sub-events) within the body of an eruptive signal. By identifying each sub-event it is possible to track the evolution of an eruption.

Santiaguito eruptions are complex, and the corresponding infrasound is relatively long in duration (10s of s) and is generated over a source area that is large (~ 200 m) compared to the characteristic acoustic radiation wavelength (e.g., 120 m for 3 Hz energy). Sound waves from Santiaguito's large and distributed vent region radiate asymmetrically. The observed waveforms not only vary in arrival time but also in appearance across the network, leading to differences in the number of correlated sub-events. The waveform variations make it necessary to locate distinct sub-events for each eruption, as a single event location does not accurately represent the entire spatial extent of the eruption.

ACKNOWLEDGEMENTS

I would like to thank my advisor Jeff Johnson for all of his help throughout this process. I would also like to thank Rick Aster for his advice and finally Bill McIntosh for all of his advice and friendship.

Special thanks go to Omar Marcillo, Julian Chaput, Hunter Knox, and Jonathan MacCarthy for helping with various aspects of my thesis.

The DEM image was courtesy of the Japanese International Development Agency (JICA), Instituto Geografico Nacional (IGN), Instituto Nacional de Sismologia, Vulcanologia, Meteorologia e Hidrologia (INSIVUMEH), and Secretaria de Planificacion y Programacion de la Presidencia (SEGEPLAN). 2003. Estudio del establecimiento de los mapas basicos y mapas de amenaza para el sistema de informacion geografica de la Republica de Guatemala. Final Report.

Partial funding was provided by the National Science Foundataion grant (NSF EAR 0738802).

RT-130 data loggers and seismic sensors were provided by IRIS PASSCAL.

TABLE OF CONTENTS

ABSTRACT.....	i
ACKNOWLEDGEMENTS.....	ii
TABLE OF CONTENTS.....	iii
LIST OF TABLES.....	iv
LIST OF FIGURES.....	v
INTRODUCTION.....	1
BACKGROUND.....	5
METHODS.....	10
Instrumentation.....	10
Data Processing.....	11
Source Localization.....	16
Sub-event Analysis.....	18
Sensitivity Study.....	30
Error Analysis.....	34
Video Analysis.....	37
DISCUSSION.....	40
CONCLUSION.....	44
REFERENCES.....	48
Appendix 1.....	53

LIST OF TABLES

Table 1. Catalog of all events	12
Table 2. Results of sensitivity study	34

LIST OF FIGURES

Figure 1. Map of Central America showing Guatemala (outlined in red) and Santiaguito Volcano (red icon).	5
Figure 2. Tectonic map of Central America centered on Guatemala (blue) and Santiaguito Volcano (red volcano symbol).....	7
Figure 3. Photo of the Santiaguito dome complex viewed from Santa Maria showing El Caliente on the far left and El Monje on the far right.....	9
Figure 4. Topographic map of Santiaguito Volcano.....	10
Figure 5. Figure showing the number of sub-events plotted against the sub-event time density for every event.....	14
Figure 6. Normalized waveform from each station (CAR, CAL and DOM) for a short duration event on January 3, 2009 at 08:22:40 UTC	19
Figure 7. Normalized waveform from each station (CAR, CAL and DOM) for a long duration event on January 1, 2009 at 20:54:30 UTC	20
Figure 8. Example correlogram for synthetic signals consisting of two distinct synthetic events shown at 3 and 9 s, representing two geographically different source locations recorded at two stations.	21
Figure 9. Correlogram from a characteristic long duration event on January 3, 2009 at 08:22:40	22

Figure 10. Sub-event locations for the long duration event on January 3, 2009 at 08:22:40	23
.....	
Figure 11. Correlogram from a characteristic short duration event on January 1, 2009 at 20:54:30	25
.....	
Figure 12. Location plot for the event on January 1, 2009 at 20:54:30	26
.....	
Figure 13. Zoomed in correlogram showing two spurious events with lag times of about - 0.5 s	27
.....	
Figure 14. Correlogram showing a long duration eruption with multiple short duration events scattered throughout the sequence on January 2, 2009 at 10:30:00 UTC	28
.....	
Figure 15. Sub-event locations for the mixed type of event on January 2, 2009 at 10:30:00	29
.....	
Figure 16. Sub-event locations for all 53 eruptions during the study period	31
.....	
Figure 17. Consistency error location plot showing sub-events from all 53 eruptions for different consistencies	35
.....	
Figure 18. Velocity error location plot showing sub-events from all 53 eruptions for different velocities	36
.....	
Figure 19. Video sequence and locations for an eruption on January 4, 2009 at 14:09:00 UTC	39
.....	
Figure 20. Histogram showing the geographic ratio for long and short duration events	42

This thesis is accepted on behalf of the faculty of the


Institute by the following committee:



Jeffrey B. Johnson, Advisor 8/28/09
Date



Richard C. Aster, Committee Member 7/30/09
Date



William C. McIntosh, Committee Member 7/30/09
Date

I release this document to the New Mexico Institute of Mining and Technology.



Kyle Richard Jones 8/28/09
Date

INTRODUCTION

Volcanologists are looked upon to supply local and national governments with accurate assessments of active and potentially active volcanoes. Currently this is done with an assortment of geophysical tools such as strain meters, seismometers, GPS, radar, etc. In recent years a new type of volcano monitoring technique has made its way into mainstream science. Acoustic surveillance has become more common among volcano researchers, [*Garces et al.*, 2003; *Johnson et al.*, 2004a; *Johnson*, 2007; *Johnson et al.*, 2008a; *Jones et al.*, 2008; *Matoza et al.*, 2007; *Petersen et al.*, 2006; *Ripepe and Marchetti*, 2002; *Sahetapy-Engel et al.*, 2008], because it provides additional source constraints beyond seismic, geodetic, remote sensing, gas and thermal measurements. Acoustic methods compliment these data because they are sensitive to volcanic unrest in frequencies that can potentially go unnoticed by many of these technologies [*Johnson et al.*, 2004a].

Broadband seismometers, global positioning system (GPS), interferometric synthetic aperture radar (InSAR), and acoustic microphones operating in the infrasonic band are used to understand volcanic unrest. Although beneficial, each tool has its limitations. For example, GPS requires stations at the exact point where the measurement is needed. Seismometers can detect internal volcanic motions in the solid Earth, whereas infrasound can detect the energy after it has been transferred to the atmosphere. Thermal remote sensing requires a relatively clear field of view, while infrasound can be detected even in low visibility situations. Acoustic sensors have the benefit of being able to detect

eruptions continuously and at longer distances (several kilometers to tens of kilometers and beyond, but raypaths in the atmosphere may be very complex [*Drob et al.*, 2003]).

Infrasound monitoring is especially useful in understanding the mechanics of explosive eruptions, because waves traveling through the air, particularly at distances of up to a few km, have simpler Green's functions than those for comparable seismic frequency waves traveling through rock. In this paper, infrasound sensors were used to study low frequency sound waves filtered between 0.25 and 2 Hz from Santiaguito volcano, Guatemala. Unlike seismic waves, which are strongly affected by the inhomogeneity of rock, particularly in highly heterogeneous volcanic locals, infrasound is propagated in a relatively homogeneous medium (air). Infrasound is gaining popularity as a monitoring technique, because it can easily be used to determine where and when an explosive event occurred [*Johnson*, 2005]. This is especially useful in areas that have multiple vents that cannot be monitored visually at all times [*Johnson*, 2005; *McGreger and Lees*, 2004]. Infrasound sensors can be deployed close enough to active vents to minimize most atmospheric propagation effects. Compared to seismology, near-surface sources can commonly be located with much greater spatial-temporal accuracy using infrasound.

Sound radiated by volcanic activity has been studied since the 1960's [*Wilson et al.*, 1966] but has only recently become a more common volcano monitoring technique [*Dibble*, 1989; *Hagerty et al.*, 2000; *Hurst and Vandemeulebrouck*, 1996; *Richards*, 1963; *Rowe et al.*, 2000; *Wilson et al.*, 1966]. Analysis of infrasound allows for the location of events, determining source overpressure, and estimating gas flux [*Fernandes et al.*, 2007; *Johnson et al.*, 2004a; *Vergnolle et al.*, 2004]. More recent studies have resolved source locations from various infrasound sources from a few meters to 10's of

meters using three or more sensors in network or array configurations [*Jones et al.*, 2008; *Ripepe et al.*, 2009b].

Infrasound sensors can be deployed using varying tactics. Like seismometers, infrasound sensors can be usefully deployed in arrays, networks, or as a single stand-alone sensor. Infrasound arrays are typically deployed farther away from a source than networks and the acquired data are useful for back azimuth calculations and event size measurements, although they can be influenced by propagation effects from the atmosphere such as refractions from different temperature layers [*Diamond*, 1963; *Garces et al.*, 1998]. Arrays can be deployed at safe distances (away from volcanic hazards) in areas where wind noise is significantly mitigated. This allows for more options when considering sensor placement, such as in high foliage or other sheltered areas [*Matoza et al.*, 2007]. Networks are especially valuable for event localization because of the azimuthal distribution of the sensors around a vent system and can be utilized to determine source locations from both short, impulsive eruptions (1 to 4 s) [*Johnson et al.*, 2008a; *Jones et al.*, 2008] and long-duration eruptions (50 s to 3 minutes) [*Johnson et al.*, 2004b; *Johnson et al.*, 2007]. This thesis highlights sub-event source localization achievable through network deployments around a vent. Single, stand-alone sensors cannot be used to determine back azimuth to a source or for locating events. To achieve source localization, at least 3 sensors must be used, however, using only one sensor can give a size estimation of event magnitude [*Petersen et al.*, 2006; *Vergnolle et al.*, 2004; *Vergnolle and Caplan-Auerbach*, 2004], when the source location is known. Mini-arrays of infrasound sensors with apertures of a few meters can be useful in a network configuration because

the signals from each mini-array can be summed to reduce wind noise and thus increase the quality of the signal.

Infrasound has been used to study different eruption types from volcanoes around the world, such as strombolian eruptions at Mt. Erebus, Antarctica [*Aster et al.*, 2004; *Dibble*, 1989; *Johnson et al.*, 2008a; *Jones et al.*, 2008; *Rowe et al.*, 2000], and Stromboli, Italy [*Johnson*, 2005; *Johnson et al.*, 2008a; *McGreger and Lees*, 2004; *Ripepe and Marchetti*, 2002; *Ripepe et al.*, 2009b], volcanic tremor events at Hawai'i [*Garces et al.*, 2003], and explosive eruptions at Mount St. Helens, Washington [*Matoza et al.*, 2007] and Augustine, Alaska [*Fernandes et al.*, 2007; *Petersen et al.*, 2006]. Data from an infrasound array at Soufriere Hills Volcano, Montserrat was recently used to track pyroclastic density currents as they traveled down the flanks of the volcano [*Ripepe et al.*, 2009a]. Data from a four-station infrasound array at Stromboli, Italy were used to calculate the back azimuth to the source to determine which vent was producing the eruptions [*Johnson*, 2005; *Ripepe and Marchetti*, 2002]. Also at Stromboli, data from a small aperture three-element array were used to locate sources from different vents using forward modeling of infrasonic arrivals [*Johnson*, 2005]. Because the vents were spatially distinct from one another it was possible to robustly differentiate which vent produced the eruption using either method.

This thesis focuses on tracking evolving sources from long duration eruptions from Santiaguito Volcano, Guatemala. Infrasound data from long duration events (50 s to 3 minutes) at Santiaguito, Guatemala [*Johnson et al.*, 2004b; *Johnson et al.*, 2007; *Sahetapy-Engel et al.*, 2008] are lower in amplitude (< 1 to 4 Pa at 1 km) compared, for example, to impulsive Strombolian events recorded at Mt. Erebus (5 to 120 Pa at 1 km).

Long duration events from Santiaguito have been studied previously [Johnson *et al.*, 2004b; Johnson *et al.*, 2007; Sahetapy-Engel *et al.*, 2008]; yet little has been done to actively locate the eruptions as a function of time. Using cross-correlated data from at least three infrasound sensors in a network configuration it is possible to locate spatially distinct sub-events over the course of an eruption lasting less than 10 s to over 200 s. The techniques described in this thesis are generally applicable to active volcanoes to monitor dangerous eruptions from safe distances at any time of day in near real-time.

BACKGROUND

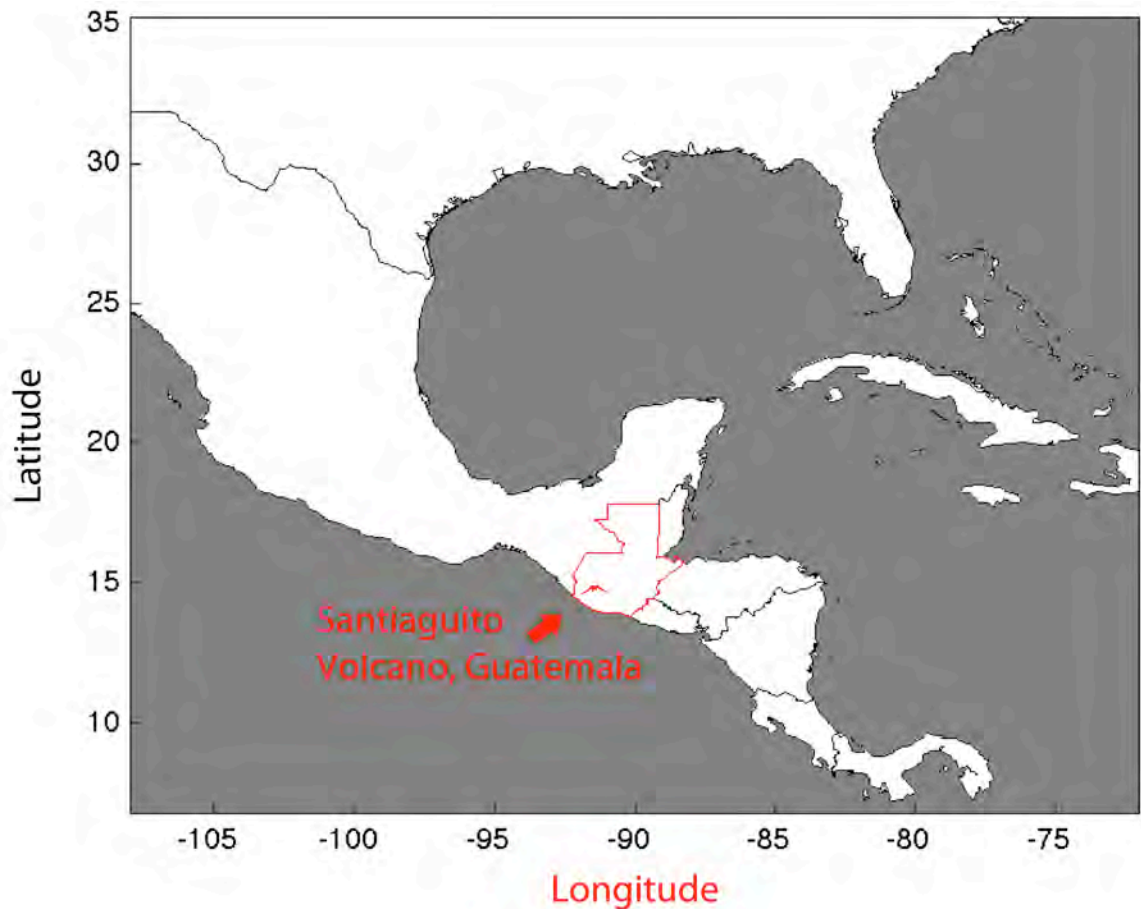


Figure 1. Map of Central America showing Guatemala (outlined in red) and Santiaguito Volcano (red icon).

Santiaguito Volcano (Figure 1) is located in southwestern Guatemala. It lies inland of an offshore trench and is considered to be part of an arc complex [Rose, 1972]. The Guatemalan forearc complex is currently moving at the same velocity as the North American forearc (Figure 2). Extension in Guatemala occurs in distinct rift structures behind the main arc and is accommodated by deformation zones between the forearc and the Caribbean plate. Extension behind the arc is considered to be a result of the interaction of the Caribbean-North American plate boundary and the Middle American Arc [Phipps Morgan et al., 2008].

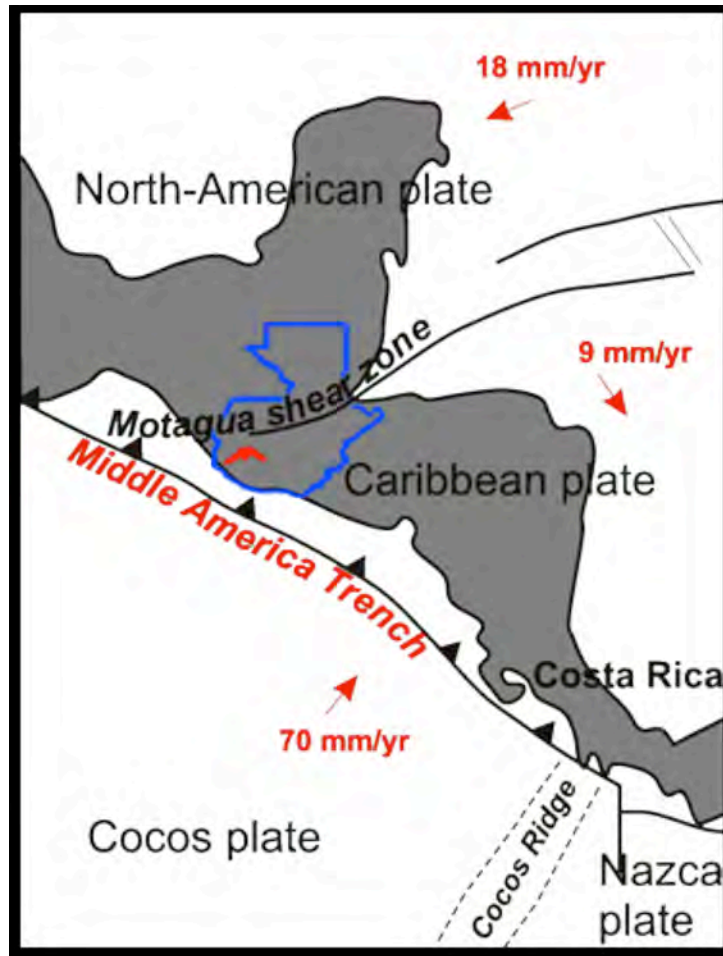


Figure 2. Tectonic map of Central America centered on Guatemala (blue) and Santiaguito Volcano (red volcano symbol). Arrows show absolute plate motion in mm/yr. [Phipps Morgan et al., 2008]

In 1902, Santa Maria volcano, Santiaguito's composite cone, explosively erupted approximately 5.5 km³ of material over a span of two days [Rose, 1972]. Periodic extrusion of the dome complex began in the explosion crater immediately following the eruption but did not erupt continuously until 1922. Currently Santiaguito Volcano is comprised of multiple domes from several vents following the start of dome-building activity. El Caliente is the central vent and La Mitad, El Monje, and El Brujo are the three

lateral vents (Figure 3). Since 1977 the majority of the activity is centered on the El Caliente vent, the original location of the 1922 eruptive sequence [*Harris et al.*, 2002; *Rose*, 1972; 1987]. The $\sim 1.1 \text{ km}^3$ extrusive dome complex lies inside the large explosion crater created by the 1902 eruption on the southwestern slope of Santa Maria Volcano [*Rose*, 1972; 1987]. Santiaguito has been one of the most active Central-American volcanoes during the past 150 years and the most active in the last 50 years [*Rose*, 1972]. There are fourteen lava and volcanic domes in this complex, which have erupted approximately 0.7 km^3 of total material between 1922 and 1972 [*Rose*, 1972]. The primary eruptive product is a calc-alkaline soda-rich dacite. [*Rose*, 1972].

Recent eruptions from the El Caliente dome are small explosive exhalations of gas and ash. They occur frequently from every five minutes to upwards of several hours. The ash columns reach heights of one to three kilometers. The ash columns erupt from ring fractures located around and within the 200-meter dacitic vent region and occasionally collapse, producing small pyroclastic density currents. Non-explosive effusive eruptions are also manifested from the dacitic block lava flow on top of the dome. [*Bluth and Rose*, 2004; *Harris et al.*, 2002].



Figure 3. Photo of the Santiaguito dome complex viewed from Santa Maria showing El Caliente on the far left and El Monje on the far right. Photo courtesy Nick Varley 2007.

Infrasound has been used regularly since 2003 to study eruption dynamics and characteristics at Santiaguito. Acoustic signals range from impulsive short duration pulses to emergent longer duration signals lasting more than 50 s. Other work at Santiaguito includes studies of thermal and heat loss of the summit crater [*Sahetapy-Engel and Harris, 2009*], long period earthquakes and dome inflation [*Johnson et al., 2008b*], SO₂ gas emissions [*Rodriguez et al., 2004*], and the evolution of phenocrysts and their melt inclusions [*Bardinizeff et al., 1980*].

METHODS

Instrumentation

The Santiaguito data analyzed here were acquired during a field deployment in January 2009. Six stations were distributed azimuthally in a network around the active Caliente vent at ranges from 330 meters to 3150 m (Figure 4). The distances are measured from the center of the vent.

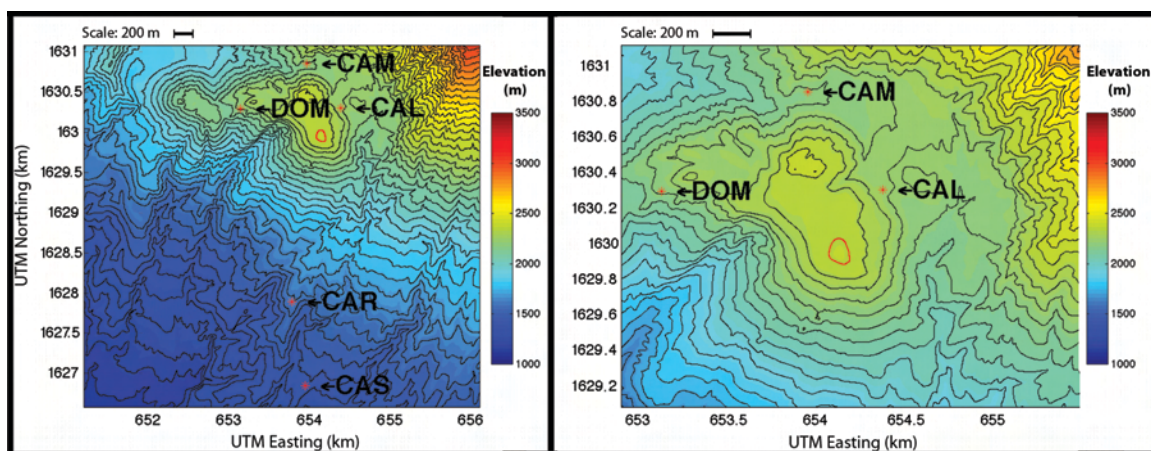


Figure 4. Topographic map of Santiaguito Volcano. (left) Each station has been located and plotted on a 30 meter resolution contour plot using coordinates from the GPS antenna at each site. **(Right)** A zoomed in plot showing the active dome area in red.

The locations for the stations were chosen based on accessibility and azimuthal distribution around the vent. Each station included one broadband seismometer (CMG 40T, 3T or 3ESP) and from one to three custom-built infrasound sensors. At stations where three infrasound sensors were present, one sensor was co-located with the seismometer and the other two were spaced up to 35 meters away from the central unit. Multiple sensors at each station provided redundancy, as well as the option to sum the signals collected from each sensor to reduce noise while processing.

Each infrasound sensor incorporates an AllSensors pressure transducer in differential mode with a dynamic range of ± 250 Pa. These sensors have a 50 micron, 2 cm-long capillary tube on one differential port creating a mechanical single-pole high pass filter (3 dB corner at 0.02 Hz) to allow barometric fluctuations in the atmosphere (microbaroms) to be equilibrated. Complete microphone specifications can be found at http://infravolc.nmtgeop.net/microphones/InfraNMT_xxC.pdf.

The infrasound data were collected using Guralp RT-130 digitizers set to record continuously at 24-bits with a gain of 32 and sample rate of 100 Hz. The entire data set contains four days of nearly continuous data.

Data Processing

Data were converted to SEG-Y format for initial analysis. The IRIS PASSCAL Quick Look (PQL) software package was used to view the raw data traces in order to pick the start times and durations of the eruptive events and compile them in a catalog (Table 1). The events that were selected for this study had amplitudes greater than 0.1 Pa to ensure high signal to noise, and durations longer than 10 s to provide sufficient signal to locate correlated sub-events.

Table 1. Catalog of all events. Events on January 1 at 20:54:30 and January 3 at 08:22:40, shown in bold italics, are the representative examples of a long and short duration event and are explained in more detail in the data analysis section.

Julian Day	Time (UTC)	Duration (s)	Amplitude (Pa)	# Sub-Events In	# Sub-Events Out	Total # Sub-Events	Geographic Ratio (%)
001	1:00:00	80	1.1	24	8	32	75
001	3:58:30	100	0.5	19	19	38	50
001	6:21:30	50	1.2	11	4	15	73
001	0:00:00	80	0.4	37	9	46	80
001	8:22:30	140	0.4	29	12	41	71
001	8:40:00	90	0.7	9	13	22	41
001	10:27:00	30	0.9	25	4	29	86
001	12:00:30	80	1.9	43	4	47	91
001	12:04:00	130	1.7	70	6	76	92
001	14:02:50	100	0.8	51	7	58	88
001	14:58:00	50	1.1	35	11	46	76
001	17:42:00	40	0.3	19	5	24	79
001	20:54:30	40	2.0	21	2	23	91
002	0:34:30	50	1.2	54	2	56	96
002	1:49:30	70	1.0	31	5	36	86
002	2:34:20	60	0.2	29	8	37	78
002	7:39:45	60	1.5	62	6	68	91
002	9:26:30	60	1.7	79	8	87	91
002	10:30:00	170	1.1	105	3	108	97
002	11:42:00	90	0.7	48	11	59	81
002	13:53:45	130	0.6	66	3	69	96
002	14:15:30	30	1.5	26	8	34	76
002	16:14:15	50	1.4	24	6	30	80
002	17:06:15	70	1.2	22	4	26	85
002	19:35:00	45	1.5	30	5	35	86

Table 1 continued

Julian Day	Time (UTC)	Duration (s)	Amplitude (Pa)	# Sub-Events In	# Sub-Events Out	Total # Sub-Events	Geographic Ratio (%)
002	23:05:30	130	0.8	127	4	131	97
003	0:09:15	50	1.7	52	4	56	93
003	0:25:30	60	1.6	61	7	68	90
003	2:02:00	20	0.7	7	2	9	78
003	5:33:00	40	0.1	16	7	23	70
003	6:18:45	190	0.9	292	5	297	98
003	7:07:30	150	0.5	169	7	176	96
003	8:22:40	150	2.3	171	3	174	98
003	9:15:00	40	0.8	11	7	18	61
003	10:40:30	30	0.2	37	4	41	90
003	12:10:30	30	0.2	13	5	18	72
003	13:49:00	130	1.0	162	0	162	100
003	18:20:40	105	2.1	30	4	34	88
003	19:40:00	60	1.6	46	7	53	87
004	0:29:50	60	1.0	21	4	25	84
004	1:06:30	100	0.9	29	9	38	76
004	3:48:30	90	2.4	60	3	63	95
004	4:52:00	50	0.2	3	5	8	38
004	5:30:00	130	3.5	72	5	77	94
004	6:35:00	12	0.3	35	4	39	90
004	6:39:00	110	0.3	123	5	128	96
004	7:50:00	20	0.4	7	4	11	64
004	9:56:00	20	0.4	8	4	12	67
004	10:16:30	70	0.7	63	2	65	97
004	11:21:00	100	0.8	82	9	91	90
004	11:24:30	14	0.2	5	3	8	63
004	14:04:00	50	0.1	9	9	18	50
004	14:09:00	140	1.1	186	2	188	99

The catalog consists of 53 events between January 1 and January 4, 2009. The events range in amplitude from 0.1 Pa to 3.5 Pa (measured as a maximum pressure amplitude at station CAR) and in duration from 12 s to 190 s. Figure 5 shows the catalog graphically as a function of the sub-event time density. The slope is sub-event time density, the number of sub-events vs. time for every event from the catalog. A high slope represents an event that has a lot of sub-events occurring in a short period of time while a low slope

suggests that the temporal density of sub-events is low over time. This shows the event catalog graphically split up by duration. There are no events during the study interval that were longer than 200 s. Forty-nine of the fifty-three events lasted between 30 and 200s.

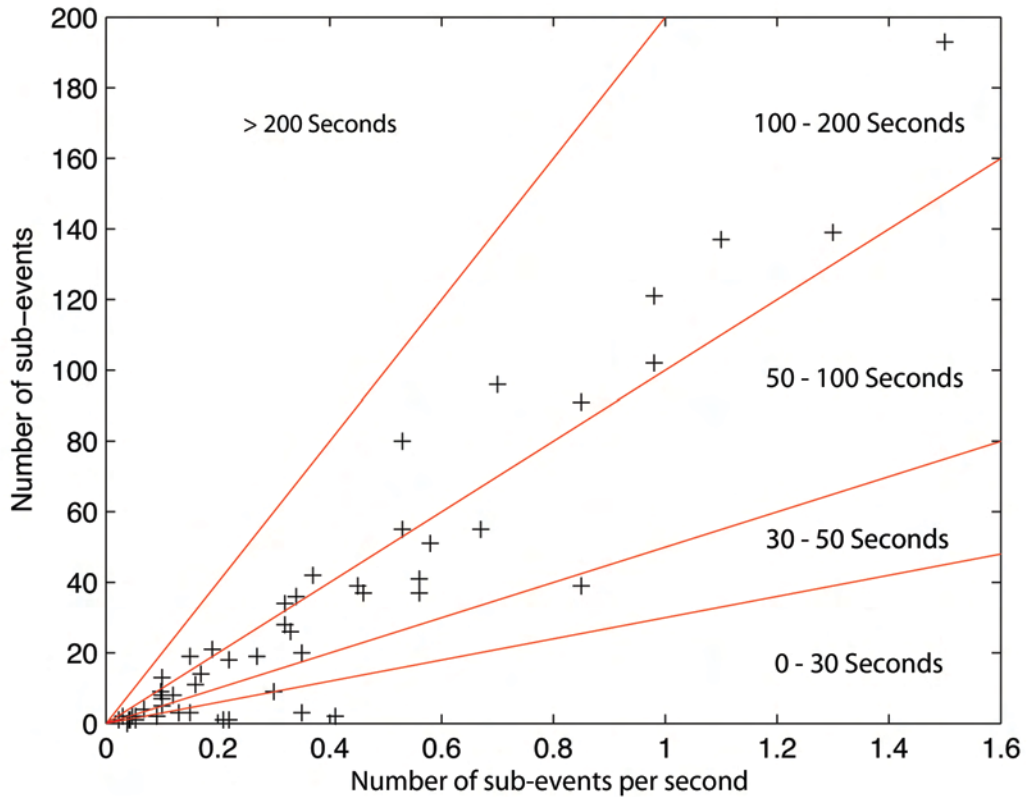


Figure 5. Figure showing the number of sub-events plotted against the sub-event time density for every event. Events with a high number of sub-events occur over longer periods of time, while the events with lower numbers of sub-events tend to have fewer sub-events per time.

A static shift is applied to the arrival times from each station to account for differences in the distance from the station to the source. Three stations (CAR9, CAL9, DOM9) were chosen because of their good azimuthal distribution around the vent region. A flat instrument response and digitizer conversion was applied to the raw signal. To convert

from the raw digital signal to pressure in Pa we use the following equation, where ΔP is excess pressure in counts:

$$\Delta P \text{ (Pa)} = \Delta P \text{ (raw)} \times \frac{\text{A to D Conversion}}{\text{Instrument Response} \frac{\text{V}}{\text{Pa}}} \times \frac{1}{\text{Digitizer Gain}} = \Delta P \times \frac{1.6 \times 10^{-6}}{21 \times 10^{-6} \frac{\text{V}}{\text{Pa}}} \times \frac{1}{32} \quad (1)$$

The following parameters were chosen based on the results of a sensitivity study (discussed later in this paper) in which parameters were varied individually to ascertain the best values for the bandpass filter, correlation window, window overlap, correlation threshold, consistency and geographic filter. These terms will now be defined.

The bandpass filter is intended to filter out portions of the signal that contain noise while enhancing the part of the signal with the most useful information. Commonly a volcanic infrasound signal is partially obscured by low frequency microbaroms from ocean waves [Bowman *et al.*, 2005] and high frequency wind noise. The correlation window refers to the number of samples used in a moving window cross-correlation. Longer windows are good at detecting longer wavelength, lower frequency events. However, in this study a short, (2 s) window is used to break up the signal and look at sub-events occurring across the entire duration of the eruption. The window overlap is the step between successive cross-correlation windows. Correlation threshold is the minimum correlation value that any sub-event must have before it can be located and must exceed the threshold for all three acoustic traces. Consistency threshold refers to the maximum number of samples that each phase lag time for each station pair can be different and still be considered a consistent, locatable sub-event. If a phase lag time does not exceed the consistency threshold then the correlated event is not consistent across each and every station pair. The geographic filter refers to a 300-meter diameter circle on the map that completely

encompasses the 200-meter vent region plus extra room for sub-events that locate near the boundaries of the vent. The 300-meter diameter circle is centered around the median value of sub-event locations for all 53 eruptions. If a sub-event is located outside this region it is considered spurious and is most likely not due to a volcanic source. These sub-events are flagged for later evaluation (and are not used in the study). It is also possible that sub-events occurring outside of the geographic filter can be indirectly related to the volcanic event being studied, such as rock fall induced by the block lava flow. While this is an indirect volcanic event, it is not the focus of this paper.

A two-pole Butterworth bandpass filter between 0.25 and 2 Hz was applied to each signal to decrease wind noise and to filter out low frequency barometric pressure disturbances. Time-domain cross-correlation was used to assess variations in phase lag. In order to identify the phase delay time between each station, CAL9 was correlated with station CAR9, DOM9 with CAL9 and CAR9 with DOM9 using a 2 s window with an overlap of 1.6 s. A correlation threshold of 0.6 was applied to every correlation value for each station pair. The same correlation must be exceeded at each station pair for a correlation to be considered robust and not randomly correlated noise. When a phase lag time exceeds both the correlation and consistency thresholds it is deemed a robust, potentially locatable, sub-event.

Source Localization

Acoustic sources are located using a modified earthquake location method by iteratively solving for the source position in the x (Easting) and y (Northing) directions while

minimizing the residual error after each iteration (e.g., earthquake location inverse problem described by [Stein and Wysession, 2003]). The linearized general acoustic inverse problem can be stated by $\Delta m = G\Delta d$. The variable Δd is the data vector of x and y direction misfits that occur at origin time (t), location $\mathbf{x} = (x, y, z)$ recorded by acoustic stations at positions $\mathbf{x}_i = (x_i, y_i, z_i)$, written as:

$$\Delta d_i = T(x, x_i) - t_i = \frac{1}{v} \left[(x - x_i)^2 + (y - y_i)^2 + (z - z_i)^2 \right]^{\frac{1}{2}} - t_i \quad (2)$$

The travel times are only dependent on the absolute value of the distances between the source and the receiver. The model adjustment parameters are represented by $\Delta m = (x, y, z, t)$, where x , y , and z are the location coordinates and t is the origin time and is constantly being updated for each iteration so that $\Delta m = G\Delta d$. For an ideal case there would be at least as many acoustic stations as there are model parameters to solve for, but there is only data from three stations and there are four parameters (x, y, z, t) to solve for. This makes the \mathbf{G} matrix underdetermined. By fixing the elevation (z) and using the three acoustic stations the \mathbf{G} matrix becomes square and invertible. This provides the best solution for a least squares fit with zero misfit. The velocity of sound waves traveling in the air is also fixed and is assumed to be 330 m/s (based on an air temperature of -2°C near the summit) and the z coordinate of the sub-event location is fixed because the elevation of the source region is known to be 2550 m based on the DEM map of the vent. With the two variables fixed, the \mathbf{G} matrix contains only the partial derivative elements of the data vector Δd (equation 2) that are being varied with respect to the model parameters Δm . The partial derivative equation for \mathbf{G} is:

$$G_{ij} = \frac{\partial d_i}{\partial m_j} \quad (3)$$

and can be expanded as follows:

$$G_{i1} = \frac{\partial d_i}{\partial m_1} = \frac{\partial d_i}{\partial x} = \frac{\partial T(x, x_i)}{\partial x} = \frac{(x - x_i)}{v} [(x - x_i)^2 + (y - y_i)^2 + (z - z_i)^2]^{-\frac{1}{2}} \quad (4)$$

$$G_{i2} = \frac{\partial d_i}{\partial m_2} = \frac{\partial d_i}{\partial y} = \frac{\partial T(y, y_i)}{\partial y} = \frac{(y - y_i)}{v} [(x - x_i)^2 + (y - y_i)^2 + (z - z_i)^2]^{-\frac{1}{2}} \quad (5)$$

$$G_{i3} = \frac{\partial d_i}{\partial m_3} = \frac{\partial d_i}{\partial t} = 1 \quad (6)$$

After each iteration the parameters were adjusted and a location was found that was better than the previous iteration's location. Each iteration's updated model parameters were fit into the forward model until the misfit data and the residual approached zero. The RMS error was computed by taking the square root of the sum of the squares of Δd . For each location the RMS error converged to zero within five iterations or less. The errors are plotted as ellipses of ± 0.02 s (2 samples) where the long axis is in the direction of least sensor coverage. The ellipses are arbitrary and do not represent the actual travel time error because the RMS error converged to zero. A more detailed discussion of this error can be found in the error analysis section.

Sub-event Analysis

Sub-events from 53 eruptions were used to locate and track evolving source locations during the eruptive events. Figure 6 and Figure 7 show three typical (normalized)

waveforms for both a long and short duration event from CAR, CAL and DOM observed during the study period.

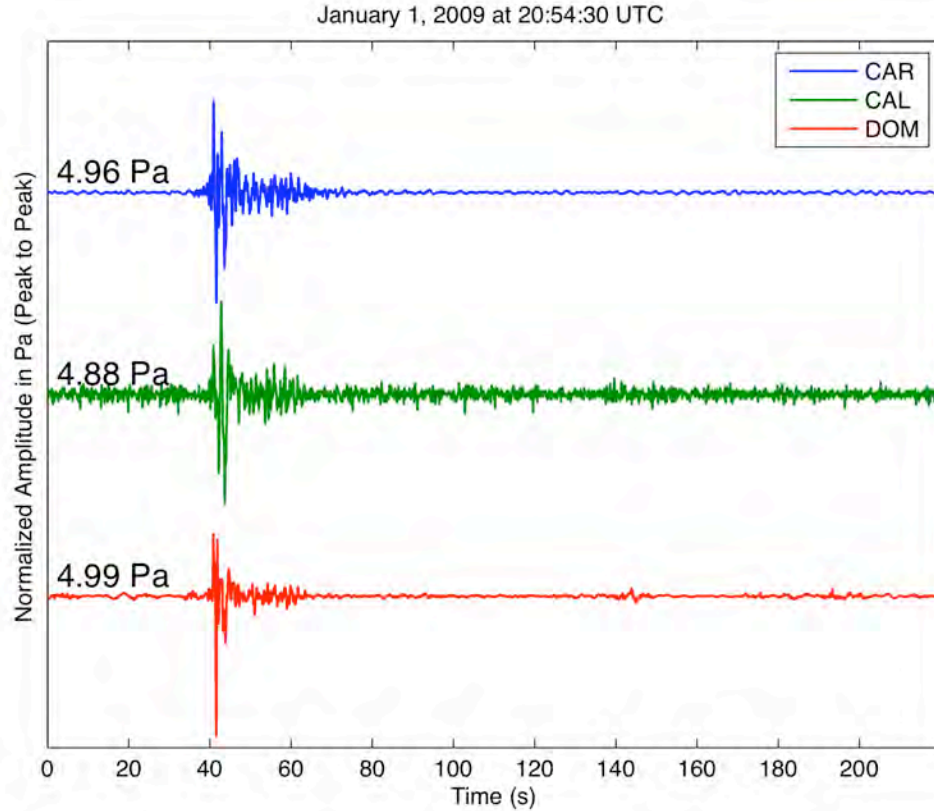


Figure 6. Normalized waveform from each station (CAR, CAL and DOM) for a short duration event on January 3, 2009 at 08:22:40 UTC. The signal has been bandpass filtered between 0.25 and 2 Hz. The numbers correspond to peak-to-peak pressure in Pa at recording site.

Well-correlated (>0.6 correlation threshold) sub-events were located for every eruption in the catalog using the methods described above. Sub-event spatial variation can be displayed graphically using a correlogram. A correlogram is a graphical representation of the phase lag time between each station pair associated with peak cross-correlation values plotted as a function of time.

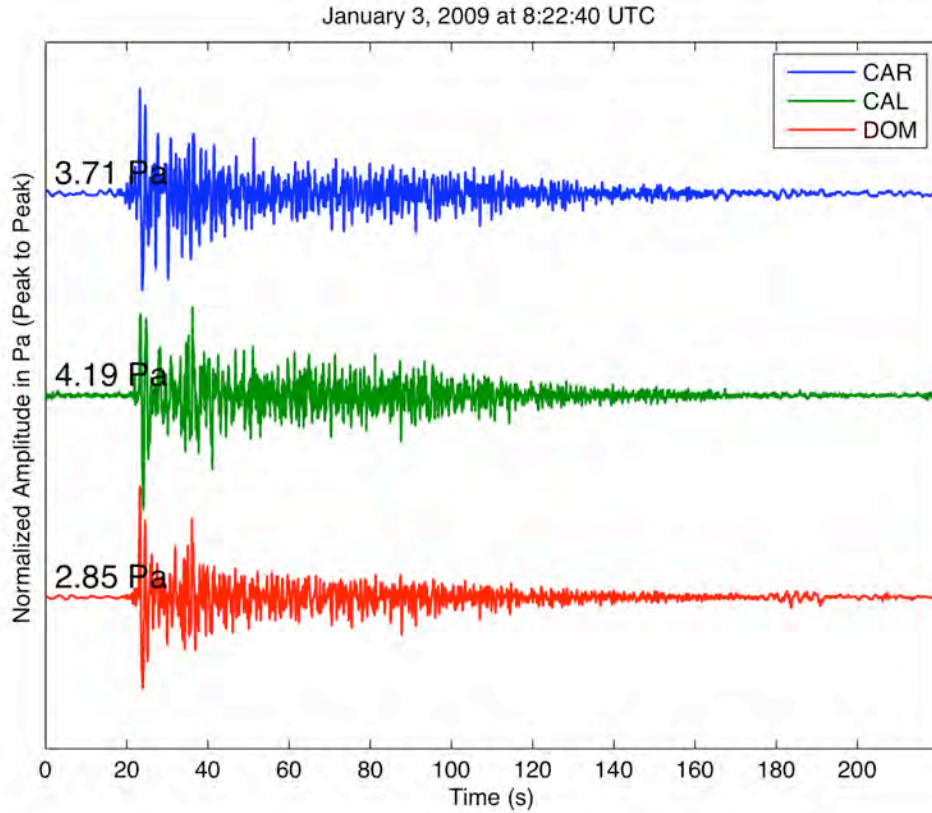


Figure 7. Normalized waveform from each station (CAR, CAL and DOM) for a long duration event on January 1, 2009 at 20:54:30 UTC. The signal has been bandpass filtered between 0.25 and 2 Hz. The numbers correspond to peak-to-peak pressure in Pa at recording site.

Figure 8 shows an example correlogram for a trace comprised of two synthetic events. The first event arrives at channel two before channel one and is graphically represented by a difference in time (lag time) of -0.25 s, shown in dark red. The color bar represents the degree of correlation between the two signals. The second event arrives at channel one ahead of channel two by 0.25 s. This means that the two events came from two geographically distinct locations.

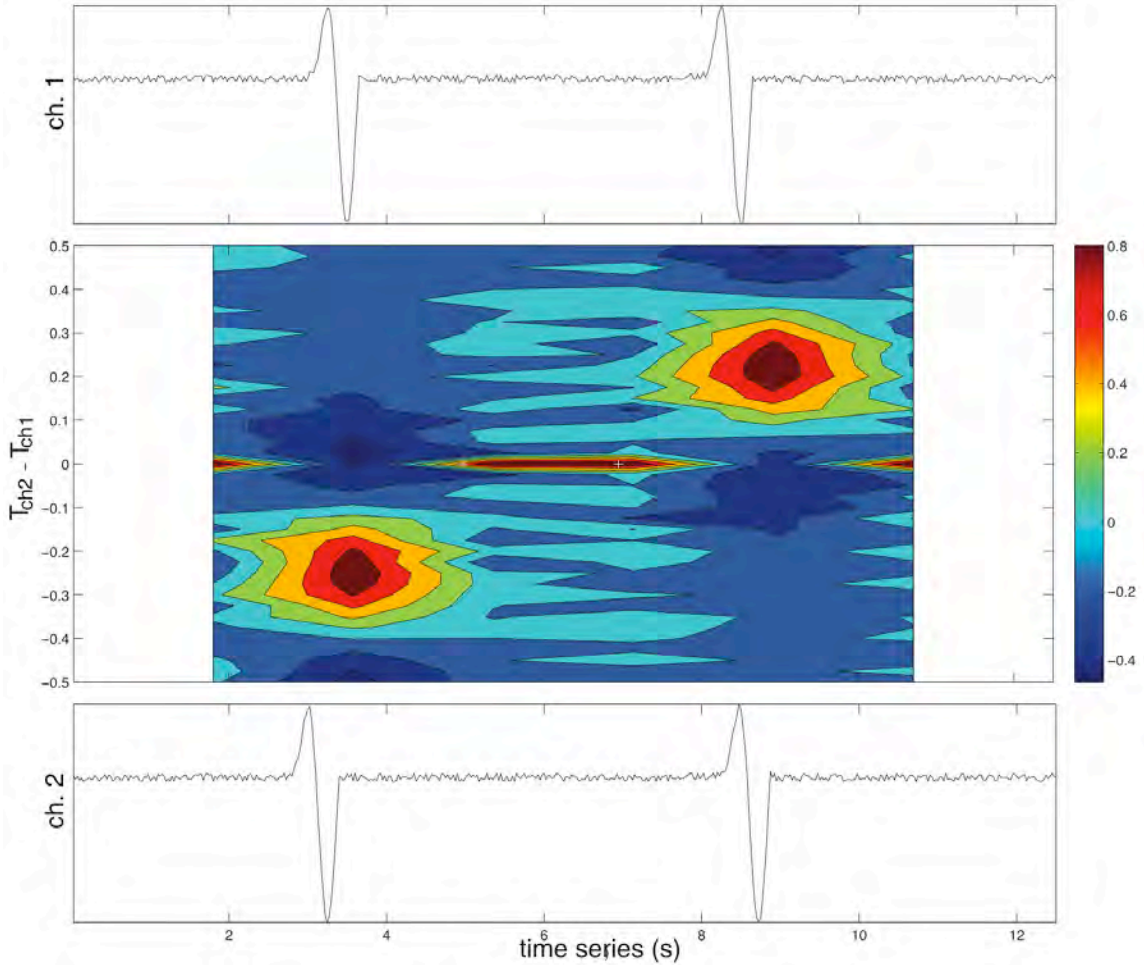


Figure 8. Example correlogram for synthetic signals consisting of two distinct synthetic events shown at 3 and 9 s, representing two geographically different source locations recorded at two stations.

By using the lag times from at least three station pair correlations it is possible to “triangulate” the source of each sub-event and spatially locate it. The correlogram for the long duration event on January 3 at 08:22:40 (Figure 9) shows a long (120 s), well-correlated (threshold greater than 0.6) signal.

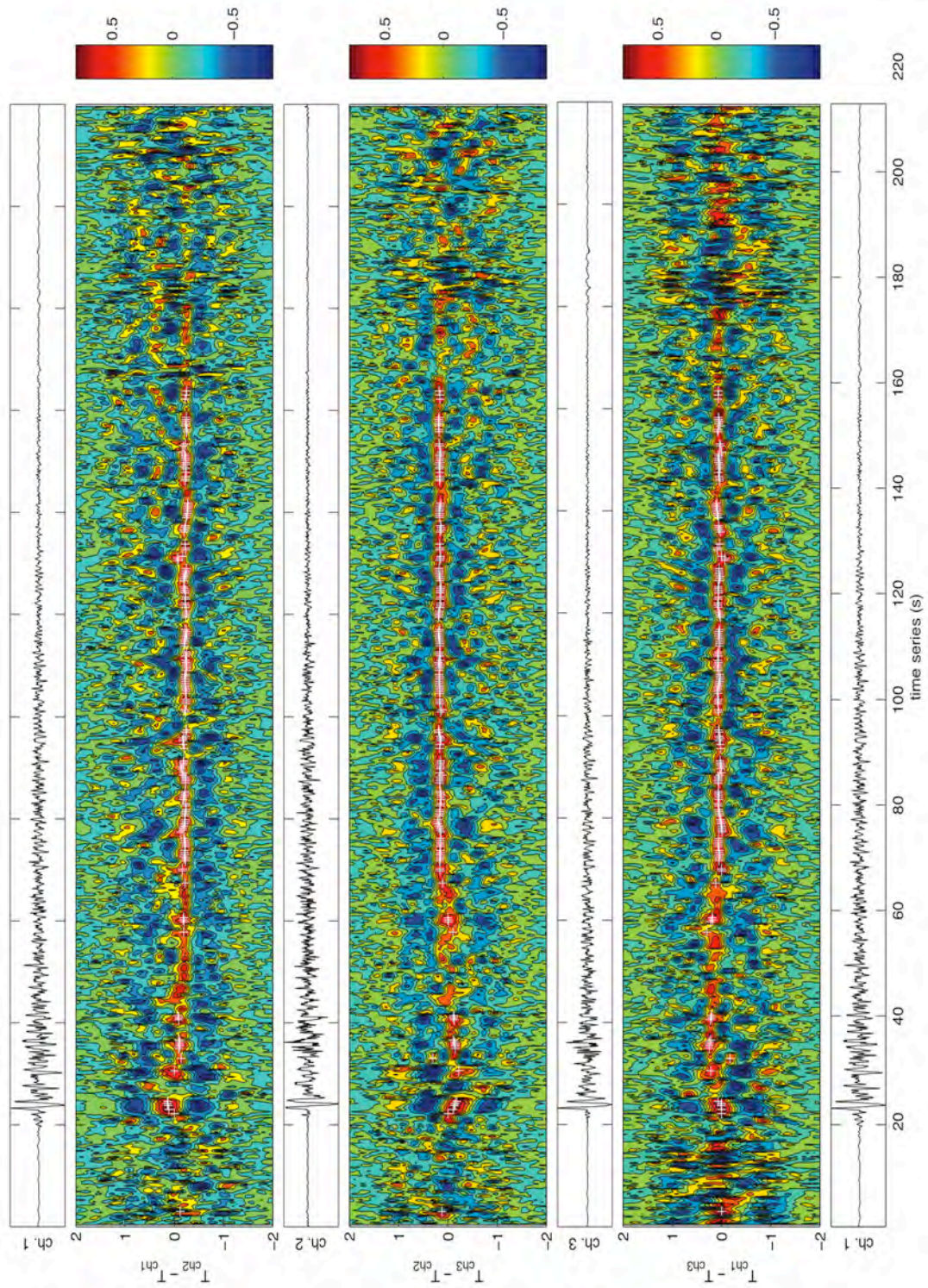


Figure 9. Correlogram from a characteristic long duration event on January 3, 2009 at 08:22:40. The three time lag delay plots show varied sub-event locations at the onset of the eruption and evolve into constant sub-event locations shown by white plus signs.

The long duration correlogram shows a sharp onset and higher amplitude relative to the rest of the signal. The correlated sub-events are not consistently locating in one position until ~50 s after onset (Figure 9). The lag times for this event only vary by about ± 0.2 s (~70 m) as shown by the correlogram and corroborated by relatively tight locations on the location map (Figure 10).

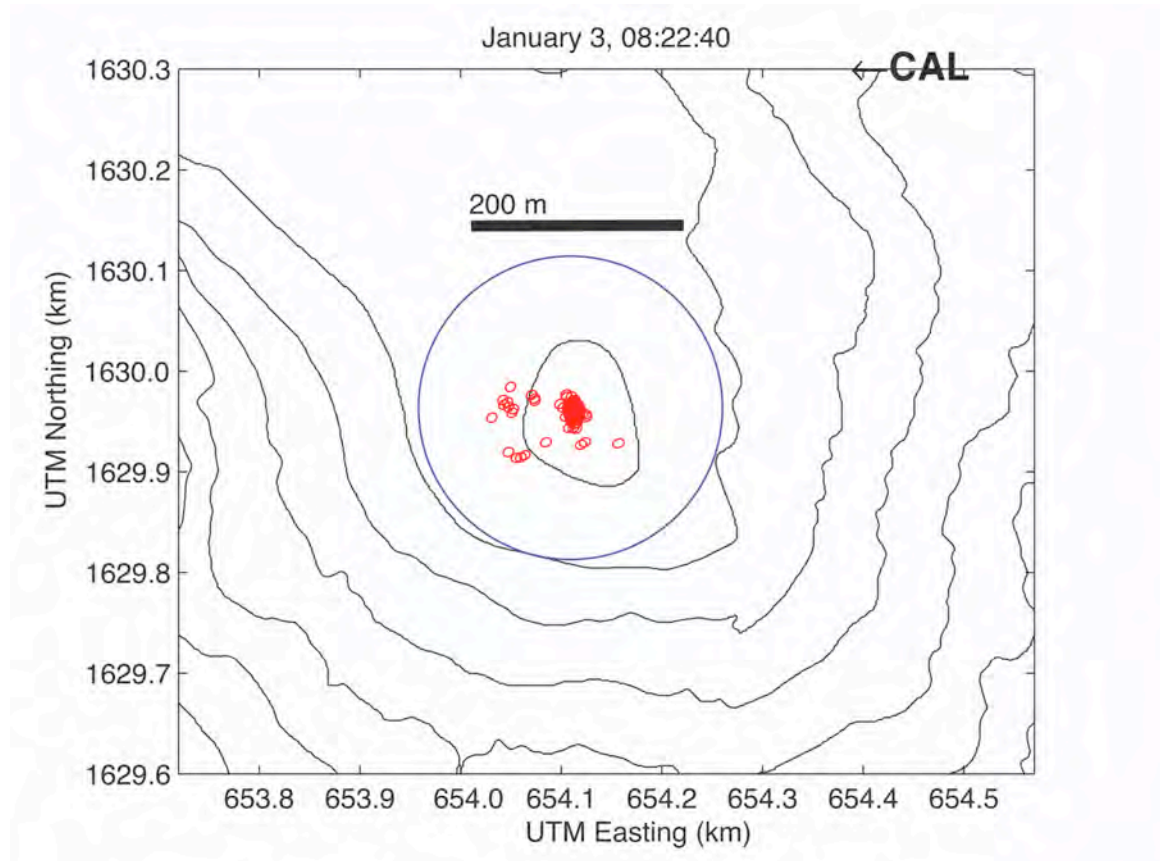


Figure 10. Sub-event locations for the long duration event on January 3, 2009 at 08:22:40. Map contour is 50 meters and the blue circle is the 300-meter diameter geographic filter.

In contrast to the numerous and well correlated sub-events from the long duration eruption, the short duration eruption shows more scatter in both the lag times as well as the corresponding sub-event locations. The short duration correlogram for an event on January 1, 2009 at 20:54:30 shows a sharp onset, high amplitude (compared to the rest of the signal) eruption that fades to background levels within 30 s after onset. The correlogram also shows that there are fewer correlated sub-events compared to the long duration event (Figure 11). The decreased number of locatable sub-events is partially due to the overall duration of the signal. It could also be because the parameters for this study were chosen such that they would apply to both long and short duration events instead of using separate parameters for each event type. This is explained in more detail in the discussion section.

The waveforms from short duration events do not correlate as well as the coda portion of the signal from long duration events. The lag times for the short duration event vary by ± 0.5 s as seen in the correlogram and in the sub-event location plot (Figure 12).

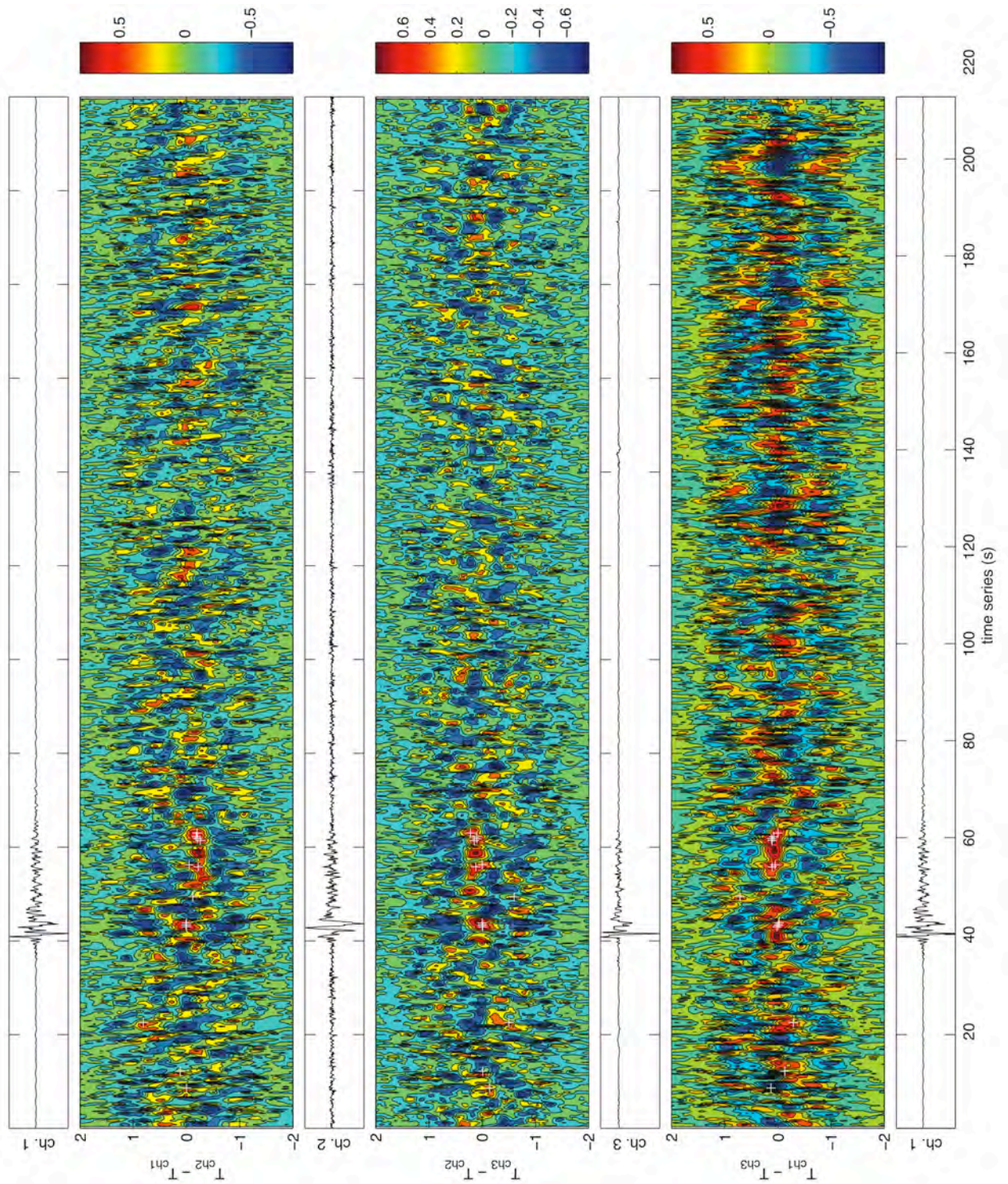


Figure 11. Correlogram from a characteristic short duration event on January 1, 2009 at 20:54:30. The correlogram shows fewer correlated lags during the short extent of the event.

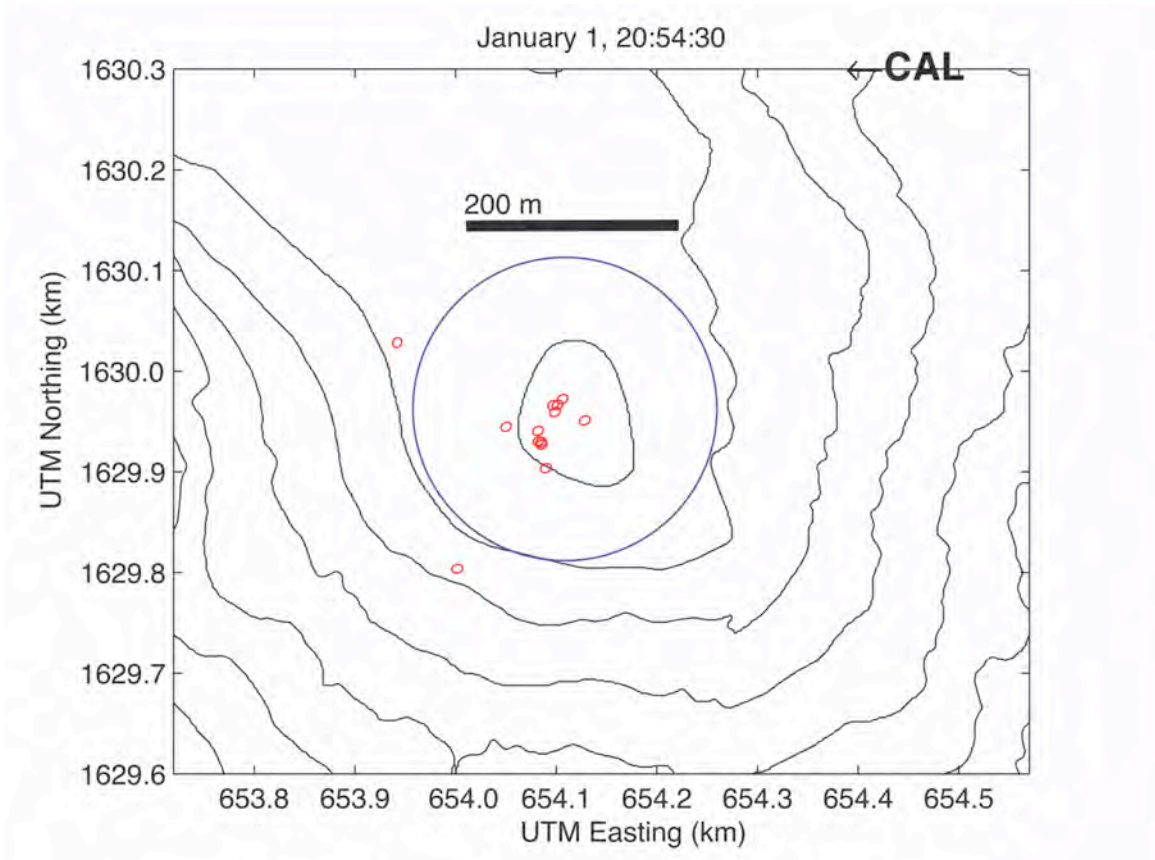


Figure 12. Location plot for the event on January 1, 2009 at 20:54:30. There are fewer sub-event locations due to the short duration of the signal and low number of correlated lag times. Map contour is 50 meters and the blue circle is the 300-meter diameter geographic filter.

The two sub-event locations that lie away from the main cluster are considered to be spurious events. When shown on the correlogram they have a delay time of about -0.5 s. The two spurious sub-events are shown on the correlogram at times 22 and 40 s (Figure 13).

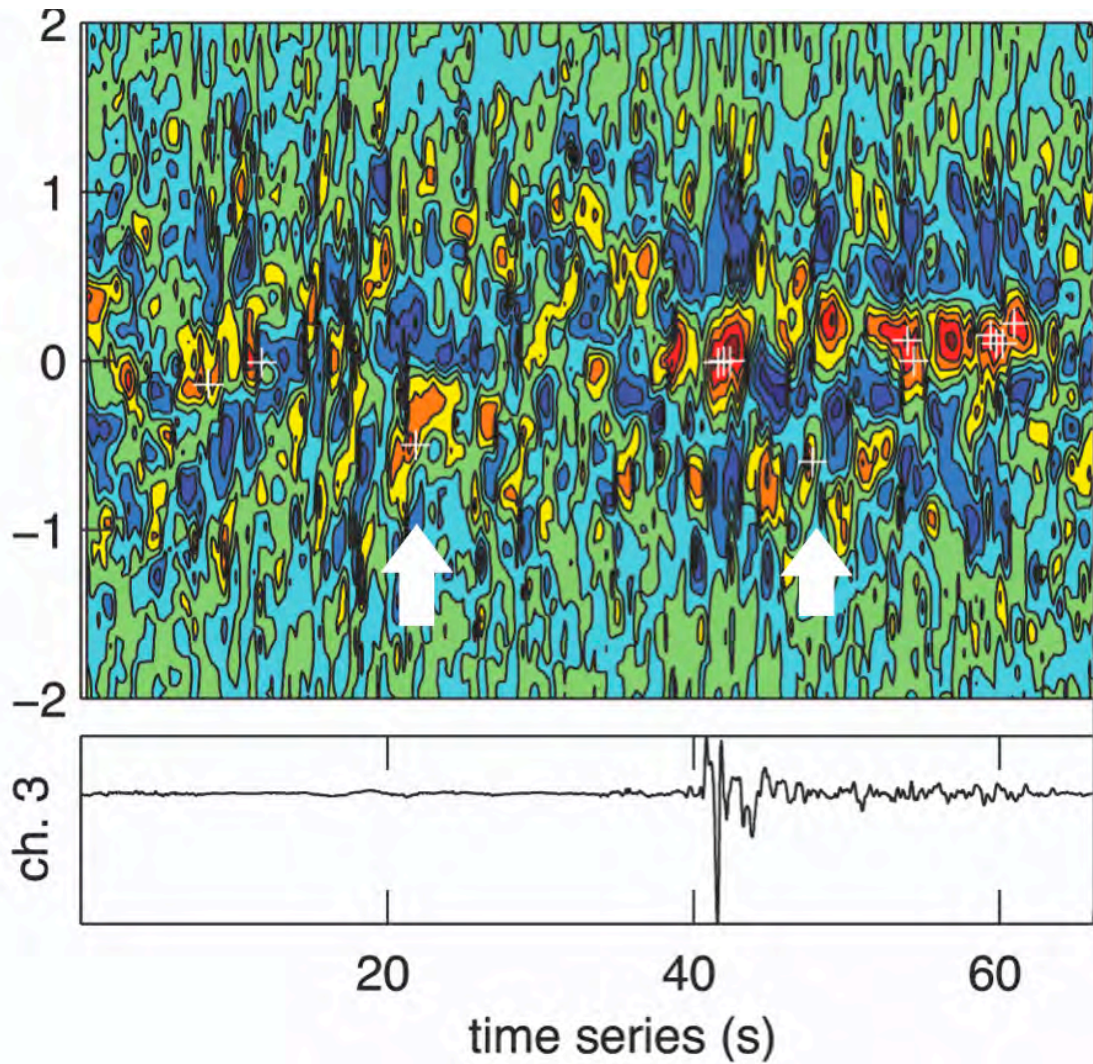


Figure 13. Zoomed in correlogram showing two spurious events with lag times of about -0.5 s. This could be an artifact of the window length during cross-correlation.

A third style of event has also been observed at Santiaguito. This multiple or mixed type of event is identified when an eruption has characteristics of both long and short duration events (Figure 14). The mixed type of events are long duration events that appear to have short duration impulsive signals scattered throughout the length of the event.

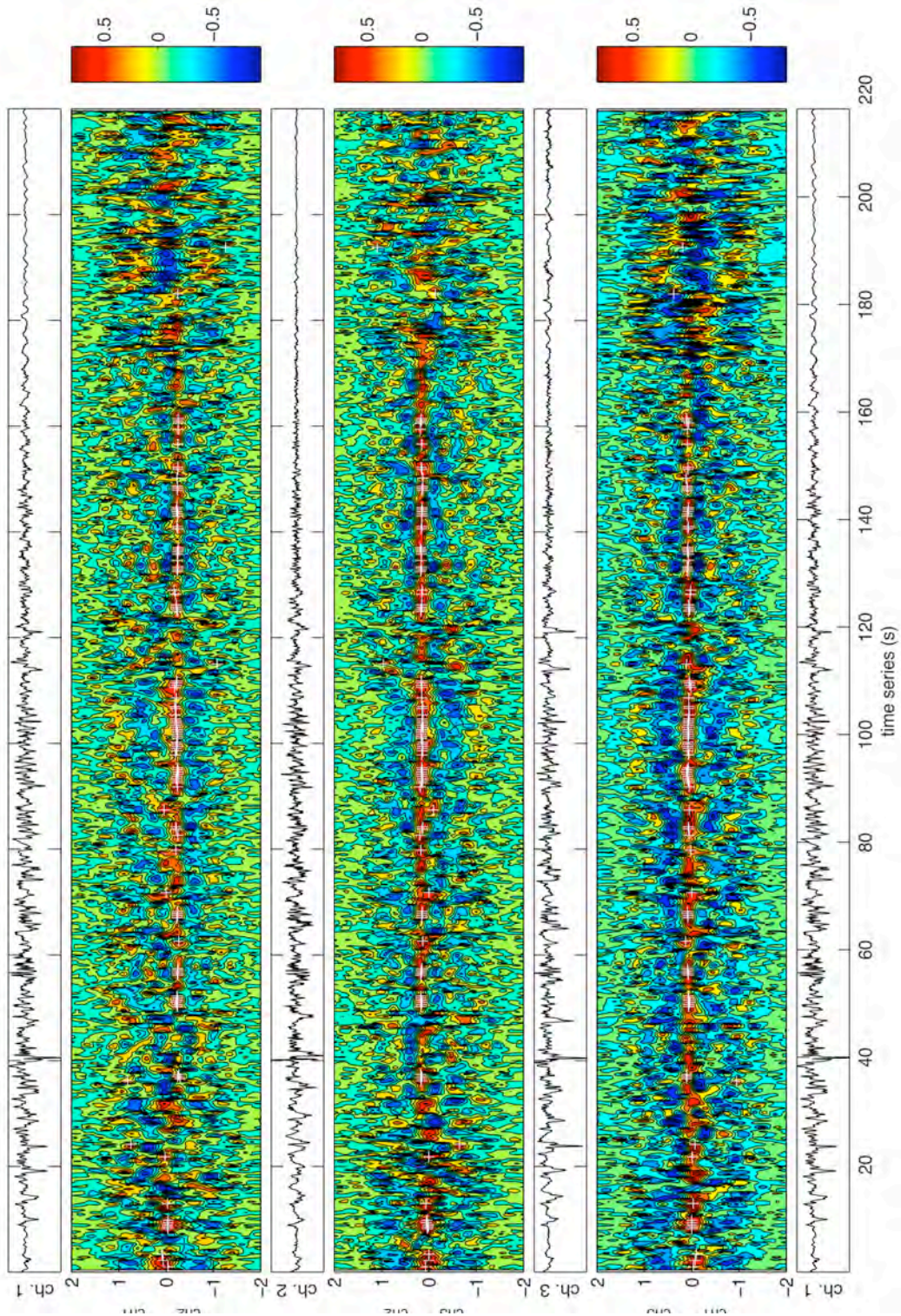


Figure 14. Correlogram showing a long duration eruption with multiple short duration events scattered throughout the sequence on January 2, 2009 at 10:30:00 UTC.

The locations for the mixed type of event show a degree of scatter over the extent of the vent region (Figure 15). In this case there are two distinct clusters of sub-events. One cluster could correspond to the impulsive portion of the signal and the other could represent the long duration nature of the signal.

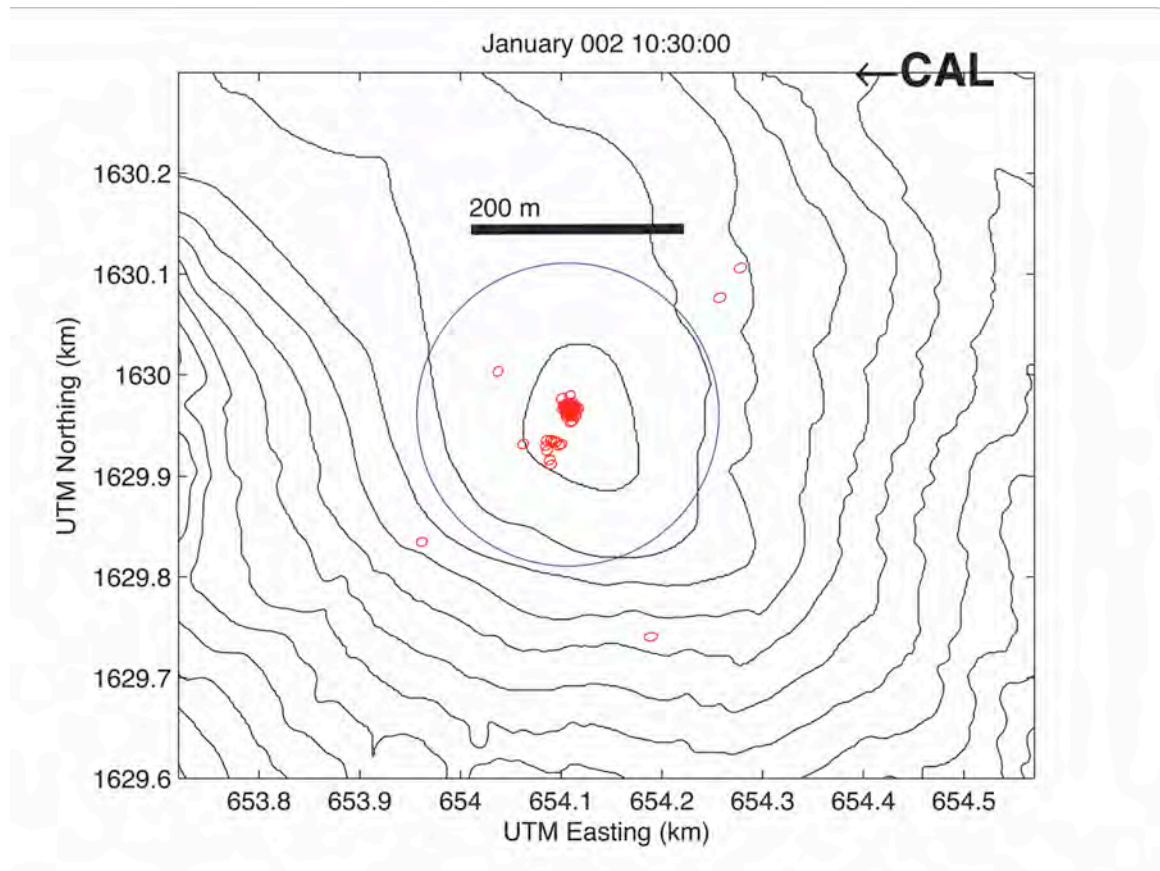


Figure 15. Sub-event locations for the mixed type of event on January 2, 2009 at 10:30:00. Map contour is 50 meters and the blue circle is the 300-meter diameter geographic filter.

Sensitivity Study

The goal was to achieve a standard parameter set that would result in a high percentage of accurate sub-events locations inside a 300-meter diameter geographic filter around the vent region for long and short duration events, as well as events displaying characteristics of both. The metric for determining the quality of the sub-event locations will be the geographic ratio and is the percentage of sub-events locating within the geographic filter. There are many parameters that can be varied to achieve optimal sub-event locations. The parameters include, bandpass filter, correlation threshold, correlation window, correlation window overlap, and consistency threshold. Assessment of the parameters was determined by analysis of sub-events that were mapped inside and outside of the geographic filter corresponding to the vent region. This was done to minimize spurious locations and maximize the number of volcano related sub-events. The geographic filter was designed by determining the median location of sub-events from all 53 eruptions.

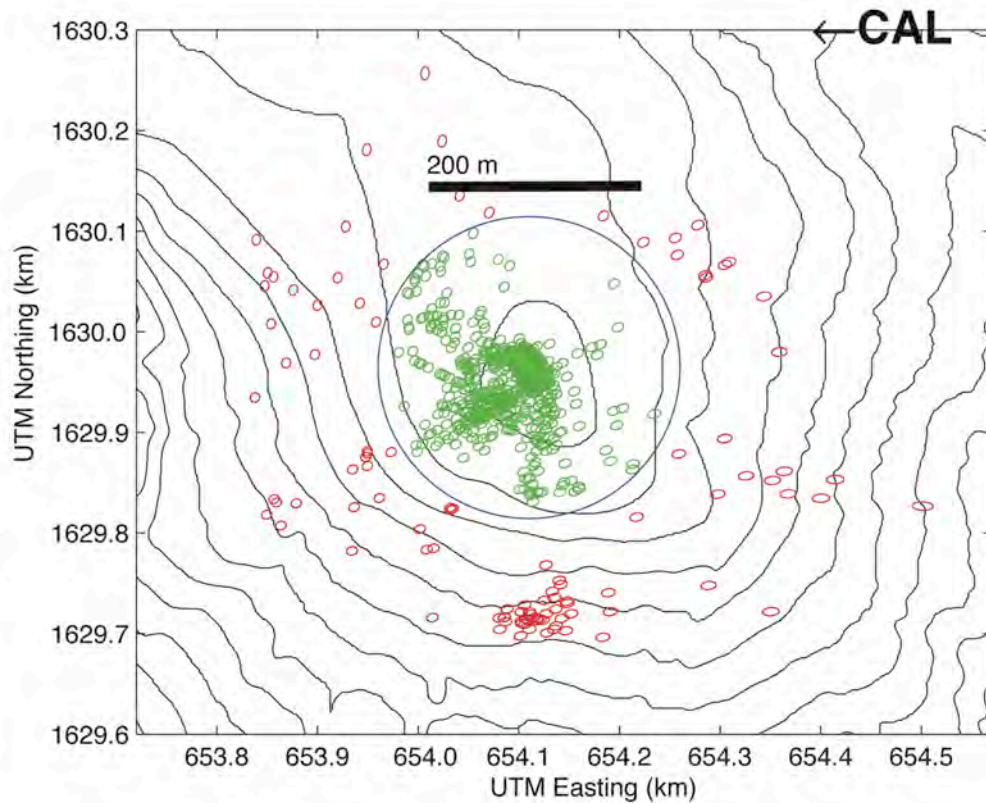


Figure 16. Sub-event locations for all 53 eruptions during the study period. The 300 meter diameter circle is centered around the median of all plotted events and encircles the 200 meter vent region. Events locating within the circle are plotted in green while any event plotting outside of the circle is shown in red. Map elevation contour is 50 meters.

All of the parameters were held constant (Table 2) except for the bandpass filter frequencies. The bandpass filters ranged from 0.125 and 20 Hz as follows: 0.125 to 2 Hz, 0.25 to 2 Hz, 0.5 to 1 Hz, 0.5 to 2 Hz, 0.5 to 3 Hz, 0.5 to 5 Hz, 0.5 to 10 Hz, 0.5 to 20 Hz, 5 to 10 Hz, and 10 to 20 Hz. The threshold was set to 0.6, the window to 2 s, the consistency to 2 and the window overlap was fixed at 0.8 for the entire study. Changing the overlap value had little to no impact on the results. The results indicate in Table 2 that while the total number of sub-events located within the geographical filter was greatest at

a filter range of 0.5 to 1 Hz, the geographic ratio was greatest at 0.25 to 2 Hz. As the lower corner frequency of the filter increased beyond 0.5 Hz the number of sub-events inside the geographical area decreased until there were no sub-events that passed the parameter criteria. A filter range of 0.25 to 2 Hz was chosen because the geographic ratio was highest at 79% for the short duration trial event. Even though the filter range of 0.5 to 1 Hz produced more events inside, it also produced more events that located outside of the geographic filter, which are treated as spurious events. This frequency filter band also produced the best geographic ratio for the long duration trial event at 99% of events locating within the geographic filter.

Using the fixed bandpass filter of 0.25 to 2 Hz the correlation window value was varied from 0.5 seconds to 10 seconds by 1-second increments. For the long duration events, a window length of 0.5 or 1 second produced the highest geographic ratio at 100%, but yielded ratios of 7% and 72% respectively for the short duration event. A window length of 2-seconds was chosen because it resulted in a greater number of sub-events with a minimal number of spurious events for both long and short duration eruptions. By selecting a window length of 2-seconds the geographic ratio for the long duration event only reduced to 99% but increased the short duration ratio to 79%.

By fixing the bandpass filter and the correlation window, the consistency threshold was varied between 0.6 and 0.9. For long duration events the geographic ratio increased as the correlation threshold increased from 98% to 100% at a correlation threshold of 0.8. For the short duration event the opposite was true. The geographic ratio decreased from 79% to 0% over the same values. For both events, a correlation threshold of 0.9 resulted in no sub-events being located because the correlation threshold was too high. Even though the

geographic ratio increased to 100% for the long duration event, the actual number of sub-events decreased from 287 to 100. A correlation value of 0.6 was selected to achieve a high geographic ratio and maximize the number of sub-events.

For the consistency threshold study the three previous parameters were held constant. The consistency threshold value was varied from 1 to 3. As the consistency threshold increased, the total number of sub-events for both the long and short duration events increased. The geographic ratio for both events peaked at 2 samples. A consistency threshold value of 2 samples was chosen because both the geographic ratio and total number of sub-events was high for this value.

The results of this sensitivity study illustrate and provide justification for the parameters that were used to locate sub-events and are the best single set of parameters possible for both long and short duration events from Santiaguito. If only one type of event were used (i.e. long duration events) it would make more sense to tailor the filter to achieve the best results for that one type of event. This will result in fewer spurious events locating outside of the geographic filter. Since all of the events in this study were processed using a standard set of parameters it is possible that some sub-events fell below the minimum correlation threshold and were not located and should be explored further in future work.

Table 2. Results of sensitivity study. Conducted by fixing all of the parameters while varying one at a time to achieve the best results. The best parameters used for this paper were a broadband filter of .25 to 2 Hz, a 2 second correlation window with 80% overlap, correlation threshold of 0.6, and a consistency threshold of 2 samples.

Fixed Variables: Correlation Threshold=0.6, Window=2 seconds, Consistency Threshold=2								
Bandpass Filter	Short Duration Event January 4, 05:30:30				Long Duration Event January 3, 06:19:15			
	Total In	Total Out	Total	% IN	Total In	Total Out	Total	% IN
0.125 to 2 Hz	51	15	66	77	249	6	255	98
0.25 to 2 Hz	53	14	67	79	250	3	253	99
0.5 to 1 Hz	109	44	153	71	227	8	235	97
0.5 to 2 Hz	64	24	88	73	255	2	257	99
0.5 to 3 HZ	21	7	28	75	204	2	206	99
0.5 to 5 Hz	11	6	17	65	193	2	195	99
0.5 to 10 Hz	3	6	9	33	174	1	175	99
0.5 to 20 Hz	2	4	6	33	172	1	173	99
5 to 10 Hz	-	-	-	-	16	0	16	100
10 to 20 Hz	-	-	-	-	-	-	-	-

Fixed Variables: Bandpass Filter=0.25 to 2 Hz, Correlation Threshold=0.6, Consistency Threshold=2								
Correlation Window	Short Duration Event January 4, 05:30:30				Long Duration Event January 3, 06:19:15			
	Total In	Total Out	Total	% IN	Total In	Total Out	Total	% IN
0.5 sec	1	13	14	7	21	0	21	100
1 sec	34	13	47	72	100	0	100	100
2 sec	53	14	67	79	250	3	253	99
3 sec	53	18	71	75	271	8	279	97
4 sec	53	19	72	74	275	11	286	96
5 sec	62	22	84	74	280	14	294	95
6 sec	62	25	87	71	292	18	310	94
7 sec	67	26	93	72	302	22	324	93
8 sec	67	28	95	71	310	29	339	91
9 sec	71	31	102	70	310	33	343	90
10 sec	81	35	116	70	323	42	365	88

Fixed Variables: Bandpass Filter=0.25 to 2 Hz, Correlation Window=3 seconds, Consistency Threshold=2								
Correlation Threshold	Short Duration Event January 4, 05:30:30				Long Duration Event January 3, 06:19:15			
	Total In	Total Out	Total	% IN	Total In	Total Out	Total	% IN
0.6	45	12	57	79	287	6	293	98
0.7	21	7	28	75	223	2	225	99
0.8	0	3	3	0	100	0	100	100
0.9	-	-	-	-	-	-	-	-

Fixed Variables: Bandpass Filter=0.25 to 2 Hz, Correlation Window=3 seconds, Correlation Threshold=.6								
Consistency Threshold	Short Duration Event January 4, 05:30:30				Long Duration Event January 3, 06:19:15			
	Total In	Total Out	Total	% IN	Total In	Total Out	Total	% IN
1	42	12	54	78	235	5	240	98
2	53	14	67	79	250	3	253	99
3	57	17	74	77	303	6	309	98

Error Analysis

The error ellipses plotted for the locations in this study are not conventional errors. The plotted error ellipses of 20 ms do not represent actual error because the RMS error is zero. Instead they show the potential of an arbitrary 2-sample (20 ms) error around the absolute location. To illustrate the potential for error in timing, a standard error of 100 ms was introduced and plotted over the 20 ms error ellipses (Figure 17). An error of 20 ms

corresponds to ~6.6 m while 100 ms corresponds to 33 m. For an error of 33 m to occur a temperature change of approximately $\pm 16^\circ\text{C}$ would be necessary. This could be a valid error for eruptions that occur during the day vs. at night where the diurnal temperature varies.

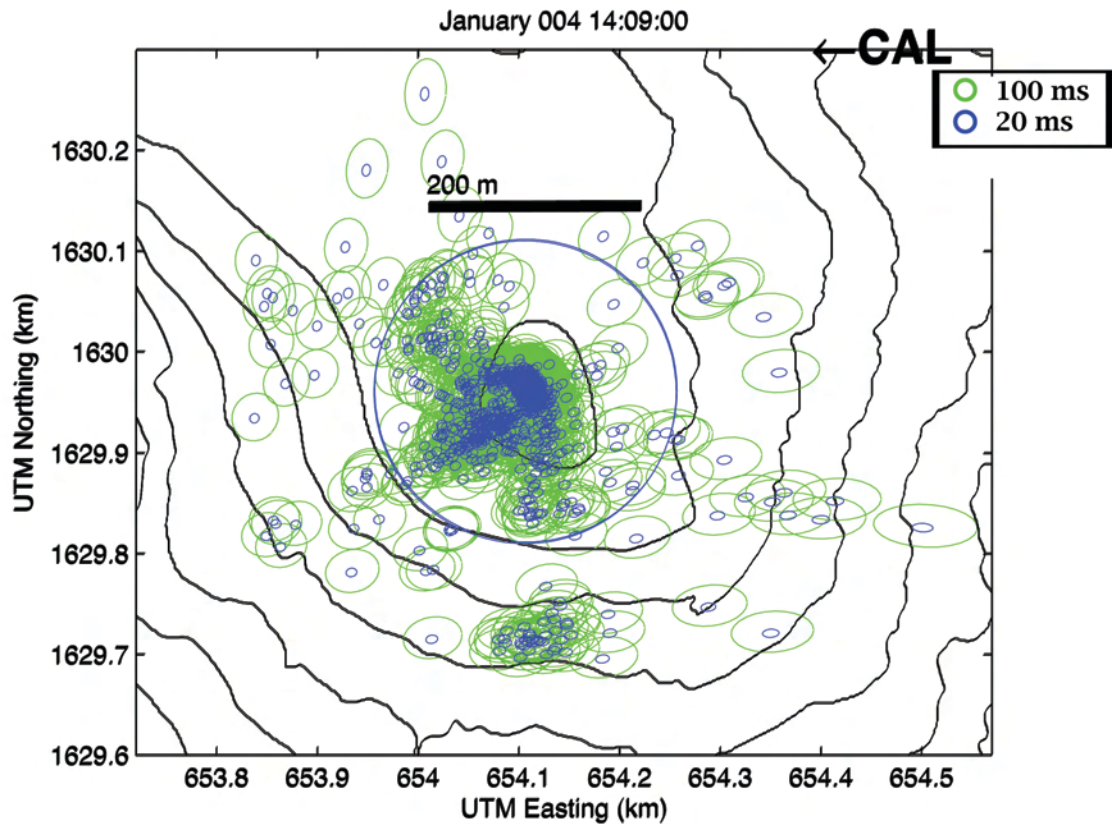


Figure 17. Consistency error location plot showing sub-events from all 53 eruptions for different consistencies. Blue ellipses correspond to a consistency of 2 samples (20 ms) and the green ellipses are for a consistency of 10 samples (100 ms).

Another way to assess error in this study is to show the effects of air temperature and sound wave velocity on the sub-event locations. This study assumes a homogeneous temperature model where the temperature does not change systematically based on the time of day or weather conditions. Figure 18 shows the sub-event locations for all 53

eruptions corresponding to different sound wave velocities. As the temperature increases from -18°C to 14°C so do the velocities (320 – 340 m/s) causing the locations to migrate in a northerly direction.

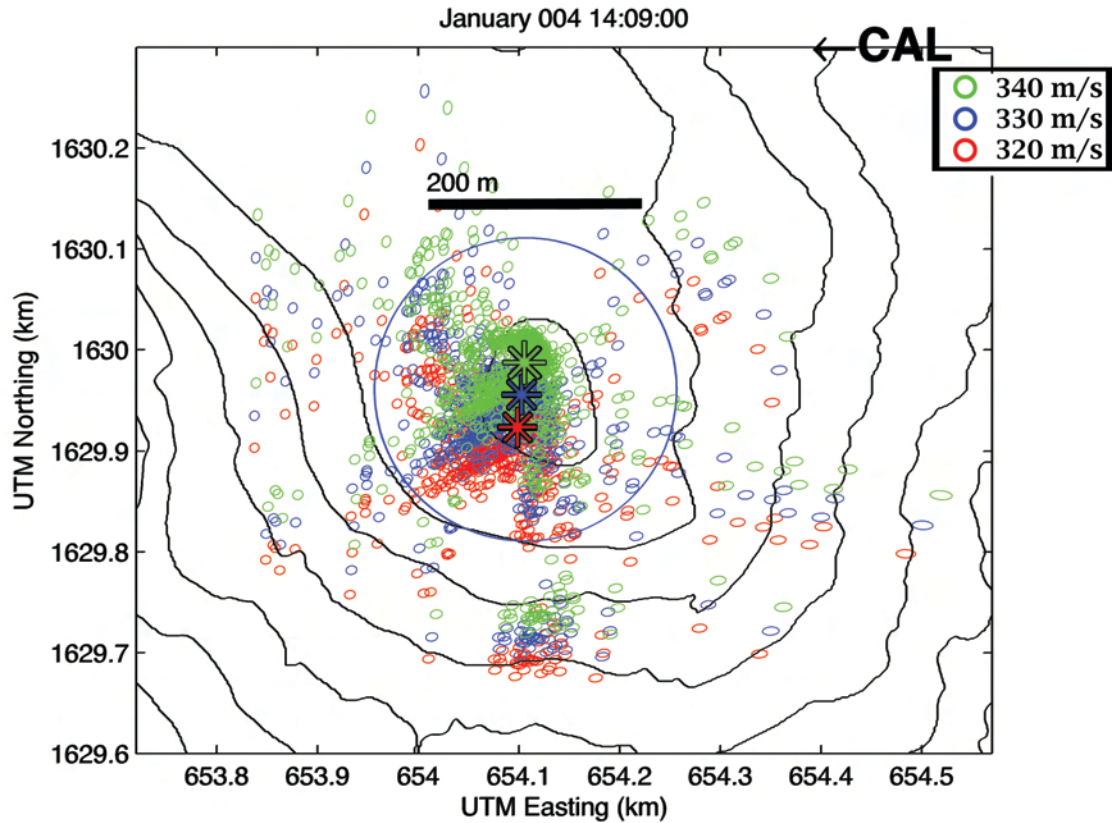


Figure 18. Velocity error location plot showing sub-events from all 53 eruptions for different velocities. Red ellipses correspond to a velocity of 320 m/s, blue ellipses correspond to 330 m/s and the green ellipses correspond to 340 m/s. The large stars represent the median values for each set of sub-event velocity locations.

In future deployments it would be useful to include atmospheric data so that the locations can be adjusted based on the temperature at any given time of day or weather condition. Figure 18 shows that the locations are strongly affected by temperature such that the median location varies by ~ 30 m for each temperature range, with a total spatial variation of ~ 60 m. Another source of temperature related error comes from the eruptive plume.

The erupting plume is much hotter than the surrounding air and will influence the velocity of the waves traveling through the plume. This would lead to differences in sub-event localization. A future study of local temperature effects would be helpful to assure the best possible sub-event locations.

When plotting all of the sub-event locations on a map a linear spatial distribution of events can be seen radiating out from the center cluster of events (Figure 16, Figure 17, Figure 18). This trend results from side lobes due to cross-correlation artifacts and finite bandwidth filtering. Peak cross-correlation values are sometimes associated with a side lobe maximum for finite band infrasound traces. These side lobe peaks radiate from the central vent region as linear spokes and are considered to be spurious sub-events. Increasing the broadband filter can help to mitigate this, however, it will affect the number of spurious sub-events.

Video Analysis

When available it is useful to utilize all available means of observation. For this study two high definition video cameras were installed on the summit of Santa Maria and used to corroborate the correlated sub-event locations. The four panel sequence below (Figure 19) is from an eruption on January 4, 2009 at 14:09:00 UTC. Each panel shows the sub-event locations at times 3, 38, 48 and 100 s after the onset of the event with the corresponding video frame for that time. The location map is oriented so that the vertical direction is aligned with the viewing angle of the camera on Santa Maria summit. The eruption starts in the upper right hand side of the map frame (panel 1). The corresponding

location is circled in the video frame. The eruption is then observed lower in the frame toward the camera (panel 2). Next, the eruption moves horizontally to the left (panel 3) and finally returns to the location from panel 2 (panel 4). The video illustrates the benefits of infrasound in spatially extensive degassing situations where the plume can obscure visual observations and make it necessary to use alternate methods to detect energy in other parts of the vent region.

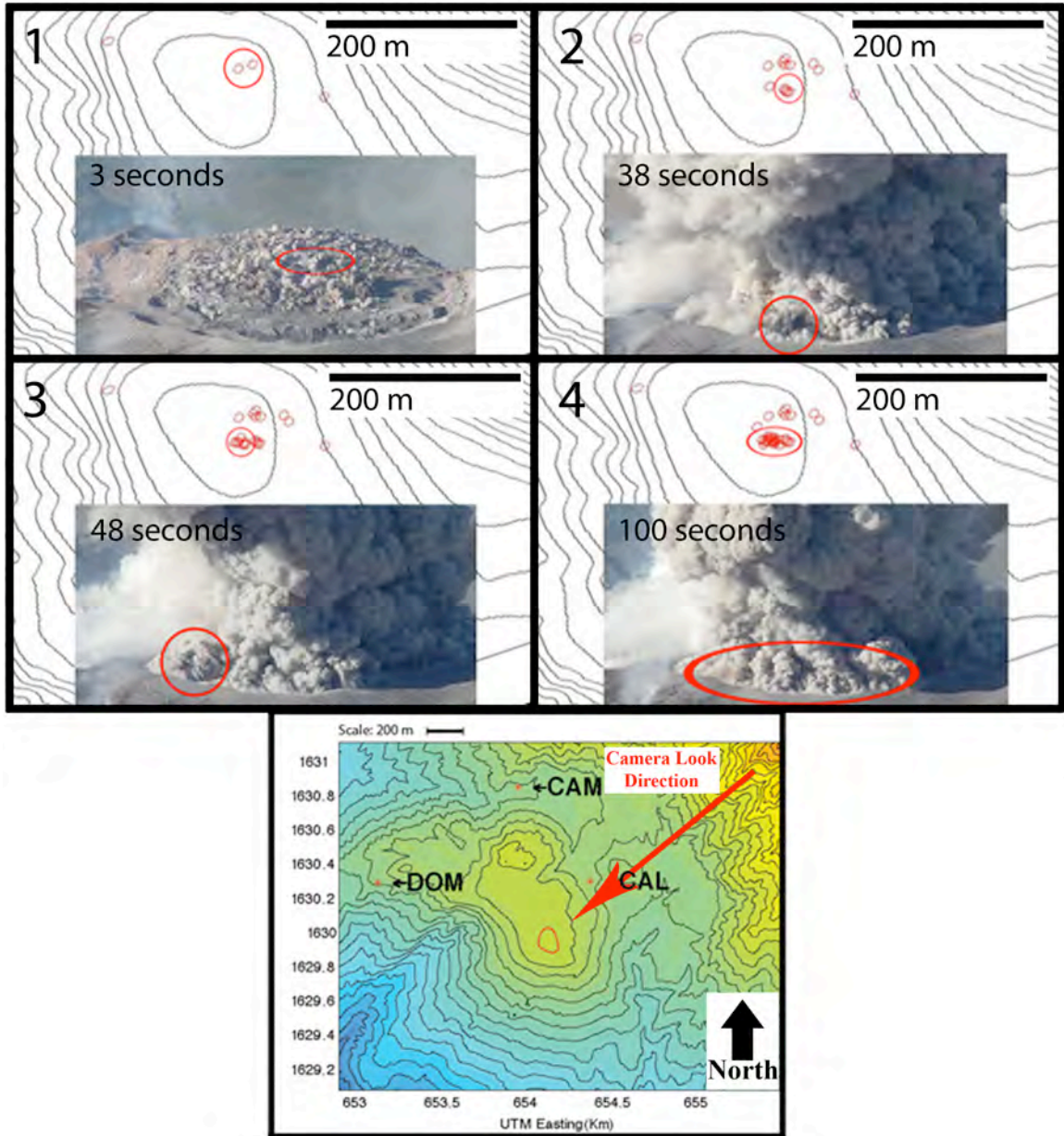


Figure 19. Video sequence and locations for an eruption on January 4, 2009 at 14:09:00 UTC. Each panel shows the sub-event locations at times 3, 38, 48 and 100 seconds with the corresponding video frame for that time. The horizontal field of view for the video screenshot is approximately 219 meters. *Panel 1.* The eruption starts in the upper right hand side of the map frame and the corresponding location is circled in the video frame. *Panel 2.* The eruption then activates lower in the frame toward the camera. *Panel 3 and 4.* The energy moves slightly to the left and finally back to the right. *Panel 5* shows the look direction of the camera. Map contour is 50 meters.

DISCUSSION

By studying the infrasound signals recorded during a field study at Santiaguito Volcano in Guatemala, two main eruption types have been identified. The first type is the short duration event. These events are typically short in duration (<50 s) and have a sharp, high amplitude onset compared to the rest of the signal. This is followed by a relatively quick decay of the signal to background levels. When performing cross-correlation of short duration events they tend to have fewer correlated sub-events. The sub-event locations for short duration events tend to be more scattered compare to the long duration events.

The long duration events typically last longer than 50 s and can have a sharp, high amplitude onset similar to the short duration event and quickly evolve into a long duration coda before fading to background levels after as much as 190 s from onset. It is interesting to note that the long and short duration events are similar because of the sharp onset, but differ where the long duration event signal quickly evolves into the highly correlated coda. Compared to the more distributed source locations from the short duration events where the gas is escaping in multiple places, it is possible that the tight clustering of events observed during the coda of the long duration events could be from the majority of gas escaping in only one spot.

Not every event recorded at Santiaguito during this study interval fits cleanly into either the long duration or short duration category. Many long duration events appear to be comprised of impulsive, short duration bursts superimposed on the long duration event. For example, some events are overall long in duration but have short duration events dispersed throughout the signal. Other events have the impulsive and large amplitude beginning of the short duration event and evolve into a very long (>50 s) event. The

infrasound indicates the succession of small explosive events during the course of a long duration eruption (Figure 14) and is an example of a mixed type event.

The character of the mixed event type suggests that there is a more complex eruptive process at work to produce a long duration event with energetic impulsive blasts throughout. There may be two methods that allow gas to escape the vent region. The first is a distributed source that allows multiple gas sources to vent simultaneously over the 200-meter region. This produces the long duration events and shows a wide distribution of sources when observed in the video records. The other method is a confined source that allows only small spurts of gas to escape episodically in a geographically confined region where the vent cannot sustain a continuous release of pressure.

The parameters discussed in the sensitivity study are optimized to find sub-events from both long and short duration events instead of short duration or long duration events only. By tailoring a set of parameters to each eruption type it is possible to increase the number of correlated sub-events that are located. Also, by decreasing the length of the correlation window and lowering the correlation threshold it will increase the number of correlated sub-events. However, this will also increase the number of spurious events that must be considered, but can be managed using the geographic filter.

There appears to be a fundamental difference between the long and short duration eruptions that can be seen when looking at the statistics for the geographic ratio. There are a higher number of correlated sub-events for long duration events compared to short duration events (Figure 20). This could be due to the fact that the one event is naturally longer than the other, allowing more time for correlated sub-events to be detected.

However, this may also be due to the nature of the event itself and how it is being erupted from the vent. It is possible that short duration events would be easier to locate and have fewer spurious events and better correlations because the event is very short (<50 s) and the signal is more impulsive and less complicated compared to the long duration events. This is not the case for the Santiaguito events. The average geographic ratio for both short and long duration events is 82%. This average cutoff was used to determine the percentage of both long and short duration events that are above the average geographic ratio. For the long duration events, 66% are above the average geographic ratio as compared to 33% of short duration eruptions.

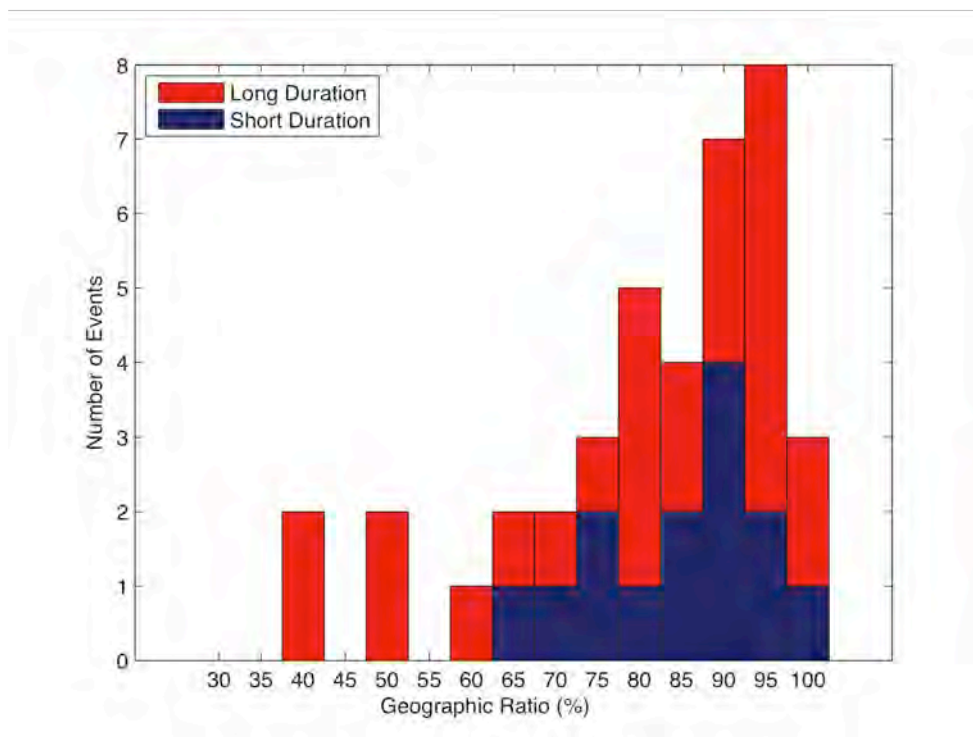


Figure 20. Histogram showing the geographic ratio for long and short duration events. There are a greater number of long duration events that have values above the average geographic ratio of 82%.

This statistic directly relates to the accuracy of the cross-correlation location program used for this study. The parameters favor long duration events and by changing the parameters, or having a separate set of parameters for each event type, it could increase the short duration geographic ratio, especially when analyzing data from other volcanoes with drastically different eruptive types.

Santiaguito eruptions can be considered complex due to the source dimensions of the vent (~200 meters) compared to the wavelength of the sound (~120 meters) radiated by the eruptions, causing the sound to radiate asymmetrically. In this case the waveform will vary not only in arrival time, but also in appearance at each station. This must be taken into consideration when using acoustic data from multiple stations at Santiaguito because the waveforms will differ between each station. This could cause a lower number of correlated sub-events. In contrast, the exposed lava lake at Mt. Erebus, Antarctica, produces single impulsive events that are easy to locate because the majority of the infrasound waves originate at only one compact location [Jones *et al.*, 2008]. With a wavelength that is large (~160 meters) compared to the dimensions of the source (<40 meters), the events can be treated as a point source [Johnson *et al.*, 2008a]. Each station will record nearly the same waveform across the network and will be easier to locate.

Jones *et al.* 2008 used a grid search method for locating impulsive events at Mt. Erebus. Because the events at Erebus are much shorter in duration than those at Santiaguito the 2-second correlation window used in this study may not be the best choice when analyzing Erebus infrasound data. Because Erebus events are treated as point sources it is acceptable to constrain the entire duration of the signal in one or two correlation windows. This would result in a single maximum correlated sub-event corresponding to

the single impulsive event. The technique described in this paper could be useful for cases when there are two or more impulsive signals very close in time. By reducing the correlation window length each pulse could be distinguished from the other and located.

When utilizing only seismic data it is possible to see that an eruption is occurring while the energy is contained in the ground, but it does not always produce an accurate location (within a few meters) on the surface once the majority of the energy is transferred to the air. When infrasound and video are used in conjunction with seismic data it becomes possible to observe that the eruptions at Santiaguito neither occur in the same location from event to event nor do they remain spatially stable during the course of one eruption. It is important to utilize video records whenever possible to ensure that the locations that are being found for each eruption are real and accurate. By utilizing these techniques it becomes possible to better understand what is occurring during long and short duration eruptions, regardless of weather, visibility or direct observation.

The technique in this paper can be applied to Erebus to identify single robust locations and in the case of Santiaguito is applied to both impulsive and long duration explosive signals to locate and track evolving source locations. While locating single impulsive events has been done in the past, tracking sub-events in long duration signals is a relatively new idea and has great application to other eruptive systems where the source vent region is spatially extensive relative to the infrasonic wavelengths.

It is important to realize that the sub-events that were located and tracked for this study represent the primary source of energy during each correlation window. When viewing many the eruptions on video the entire 200 m vent region is obscured by the plume,

indicating that gas is being released over the entire area. There could be more that is occurring during each eruption that this study was not set to observe, such as where the rest of the gas is being released and whether or not they converge to release at one point. Future research should look into how the rest of the infrasound is distributed around the vent system.

To expand on the processing part of this study there are many other parameters that can be modeled to more effectively locate sub-events. For example, this study used a simple atmospheric model that assumed a constant temperature and a homogeneous atmosphere. In reality the temperature will vary depending on the time of day as well as during the course of an eruption. The eruptive plume is much hotter than the surrounding air and will affect the propagation of the waves. The ash particles in the plume will also act to affect the velocity of the infrasound waves. Tests should be performed such that a suitable model can be used when locating these sub-events.

CONCLUSION

By utilizing time-domain cross-correlation across a three-station network it is possible to locate and track spatially and temporally evolving sub-events during eruptions at Santiaguito Volcano in Guatemala. From an infrasonic deployment in January 2009, 53 events were analyzed to determine how sources from a distributed source region evolve over time. Three acoustic stations were successfully used to locate and track sub-event sources during the course of both long (>50 s) and short (<50 s) duration eruptive events.

The events observed and analyzed for this study fell into two primary categories, long and short duration events, and a third, mixed event category. The long duration events had sharp, impulsive onsets with long, well correlated signals that lasted, in some cases, for over 150 s. In contrast, the short duration events had an impulsive onset and faded to background levels within 50 s. The long duration events had a larger number of correlated sub-events compared to the short duration events (Table 2). The long duration eruptions also had a higher geographic ratio with 66% of the long duration eruptions above the average geographic ratio. Only 33% of the short duration eruptions were above the geographic ratio (Figure 20). A third type of event observed at Santiaguito contained elements of both the long and short duration events. These mixed type of events were long in duration and contained impulsive events throughout the duration of the event. The long duration aspect of these events correlated very well with sub-events that located in tight groups similar to the standard long duration event. They also had sub-events that were more scattered because of the impulsive portion of the signal.

When using the technique from this study for sub-event localization it is important to recognize that not all events from one source are the same. There can be short duration events, long duration events, and a combination of both at any given time from the same source. As shown in Table 2, the number of sub-events that locate within the geographic filter are controlled by the parameters that are selected. By varying each parameter, the number of real sub-events increases or decreases depending on which parameter is being considered and the nature of the variation. Most of the spurious sub-events can be attributed to artifacts of the correlation process and can be disregarded. For Santiaguito there are no other sources that have been observed apart from the 200 m vent region that

could be causing consistent, correlated infrasound across the network. It is more likely that wind noise is being correlated in these cases.

The goal was to find a standard set of parameters that could be used to locate and track sub-events from all types of events. This study successfully demonstrated that a single set of correlation parameters could be chosen that both maximized real sub-events and minimized spurious locations.

Whenever possible it is beneficial to use as many instruments as are available so that the results can be corroborated by a variety of scientific methods. The video from Santiaguito illustrates the need for multiple observing techniques. It can be difficult to observe the intricate superposition of sub-events occurring during an eruption and once the column of ash obscures the opposite end of the vent region it becomes necessary to use infrasound sensors to observe the eruption. The Santiaguito video has shown that the sub-event localization technique described above can be used to accurately track an eruption as it evolves both spatially and temporally.

Infrasound is a unique and effective tool for volcano monitoring with important applications in real-time instrumentation of volcanoes in populated areas as well as purely scientific endeavors. The technique outlined in this study can not only be applied to both short and long duration events observed at Santiaguito but to other volcanoes with multiple eruptive styles around the world.

REFERENCES

- Aster, R. C., et al. (2004), New instrumentation delivers multidisciplinary real-time data from Mount Erebus, Antarctica., *EOS Trans.*, 85(10), 97-101.
- Bardinizeff, J. M., et al. (1980), Evolution of Phenocrysts and Their Melt Inclusions in the Dacite of Santiaguito Dome, Guatemala., *Comptes Rendus Hebdomadaires Des Seances De L Academie Des Sciences Serie D*, 290(12), 743-746.
- Bluth, G. J. S., and W. I. Rose (2004), Observations of eruptive activity at Santiaguito volcano, Guatemala, *Journal of Volcanology and Geothermal Research*, 136(3-4), 297-302.
- Bowman, J. R., et al. (2005), Ambient infrasound noise, *Geophysical Research Letters*, 32(9), 5.
- Diamond, M. (1963), Sound Channels in the Atmosphere, *Journal of Geophysical Research*, 68(11), 3459-3464.
- Dibble, R. R. (1989), Infrasonic recordings of Strombolian eruptions of Erebus, Antarctica, March–December 1984, covering the jump in activity on 13 September 1984, *J. Latter, Editor, Volcanic Hazards, Assessment and Monitoring, Springer-Verlag, Berlin*, 536–553.
- Drob, D. P., et al. (2003), Global Morphology of Infrasound Propagation, *J. Geophys. Res.*, 108(D21), 4680.
- Fernandes, J. J., et al. (2007), Estimates of gas flux from infrasonic signals at Augustine Volcano during the January 2006 eruption; implications for eruption plume types, *Geological Society of America, Cordilleran Section, 103rd annual meeting Abstracts with Programs - Geological Society of America*, 39(4), 78.

- Garces, M., et al. (2003), Infrasonic tremor observed at Kilauea Volcano, Hawai'i, *Geophys. Res. Lett.*, 30.
- Garces, M. A., et al. (1998), Traveltimes for infrasonic waves propagating in a stratified atmosphere, *Geophysical Journal International*, 135(1), 255-263.
- Hagerty, M. T., et al. (2000), Analysis of seismic and acoustic observations at Arenal Volcano, Costa Rica, 1995-1997, *Journal of Volcanology and Geothermal Research*, 101(1-2), 27-65.
- Harris, A. J. L., et al. (2002), The thermal stealth flows of Santiaguito dome, Guatemala: Implications for the cooling and emplacement of dacitic block-lava flows, *Geological Society of America Bulletin*, 114(5), 533-546.
- Hurst, A. W., and J. Vandemeulebrouck (1996), Acoustic noise and temperature monitoring of the Crater Lake of Mount Ruapehu Volcano, *Journal of Volcanology and Geothermal Research*, 71(1), 45-51.
- Johnson, J. B., et al. (2004a), Volcanic eruptions observed with infrasound, *Geophysical Research Letters*, 31(L14604), 1-4.
- Johnson, J. B., et al. (2004b), Explosion dynamics of pyroclastic eruptions at Santiaguito Volcano, *Geophys. Res. Lett.*, 31.
- Johnson, J. B. (2005), Source location variability and volcanic vent mapping with a small-aperture infrasound array at Stromboli Volcano, Italy, *Bulletin of Volcanology*, 67(1), 1-14.
- Johnson, J. B. (2007), On the relation between infrasound, seismicity, and small pyroclastic explosions at Karymsky Volcano, *J. Geophys. Res.*, 112.
- Johnson, J. B., et al. (2007), Eruption dynamics at the active Santiaguito Dome inferred

- from a multidisciplinary geophysical experiment, *Geological Society of America, Northeastern Section, 42nd annual meeting*.
- Johnson, J. B., et al. (2008a), Acoustic Source Characterization of Impulsive Strombolian Eruptions from the Mount Erebus Lava Lake, *Journal of Volcanology and Geothermal Research*, 177(3), 673-686.
- Johnson, J. B., et al. (2008b), Long-period earthquakes and co-eruptive dome inflation seen with particle image velocimetry, *Nature*, 456(7220), 377-381.
- Jones, K. R., et al. (2008), Infrasonic tracking of large bubble bursts and ash venting at Erebus Volcano, Antarctica, *Journal of Volcanology and Geothermal Research*, 177(3), 661-672.
- Matoza, R. S., et al. (2007), An infrasound array study of Mount St. Helens, *Journal of Volcanology and Geothermal Research*, 160(3-4), 249-262.
- McGreger, A. D., and J. M. Lees (2004), Vent discrimination at Stromboli Volcano, Italy, *Journal of Volcanology and Geothermal Research*, 137(1-3), 169-185.
- Petersen, T., et al. (2006), Local infrasound observations of large ash explosions at Augustine Volcano, Alaska, during January 11, 2006, *Geophys. Res. Lett.*, 33.
- Phipps Morgan, J., et al. (2008), Intra-arc extension in Central America: Links between plate motions, tectonics, volcanism, and geochemistry, *Earth and Planetary Science Letters*, 272(1-2), 365-371.
- Richards, A. F. (1963), Volcanic sounds; investigation and analysis, *Journal of Geophysical Research*, 68(3), 919-928.
- Ripepe, M., and E. Marchetti (2002), Array tracking of infrasonic sources at Stromboli volcano, *Geophys. Res. Lett.*, 29.

- Ripepe, M., et al. (2009a), Tracking Pyroclastic Flows at Soufriere Hills, *EOS Trans.*, 90(27), 229-230.
- Ripepe, M., et al. (2009b), The onset of the 2007 stromboli effusive eruption recorded by an integrated geophysical network, *Journal of Volcanology and Geothermal Research*, 182(3-4), 131-136.
- Rodriguez, L. A., et al. (2004), SO₂ emissions to the atmosphere from active volcanoes in Guatemala and El Salvador, 1999-2002, *Journal of Volcanology and Geothermal Research*, 138(3-4), 325-344.
- Rose, W. I. (1972), Santiaguito Volcanic Dome, Guatemala, *Geol. Soc. Am. Bull.*, 83, 1413-1434.
- Rose, W. I. (1987), Volcanic activity at Santiaguito Volcano, 1976-1984, *Spec. Pap. Geol. Soc. Am.*, 212(17-27).
- Rowe, C. A., et al. (2000), Seismic and acoustic observations at Mount Erebus Volcano, Ross Island, Antarctica, 1994-1998, *Journal of Volcanology and Geothermal Research*, 101(1-2), 105-128.
- Sahetapy-Engel, S., and A. Harris (2009), Thermal structure and heat loss at the summit crater of an active lava dome, *Bulletin of Volcanology*, 71(1), 15-28.
- Sahetapy-Engel, S. T., et al. (2008), Thermal, seismic and infrasound observations of persistent explosive activity and conduit dynamics at Santiaguito lava dome, Guatemala, *Journal of Volcanology and Geothermal Research*, 173(1-2), 1-14.
- Stein, S., and M. Wysession (2003), *An Introduction to Seismology, Earthquakes, and Earth Structure*, 497 pp., pg 415-424, Blackwell Publishing Ltd.
- Vergnolle, S., et al. (2004), Acoustic measurements of the 1999 basaltic eruption of

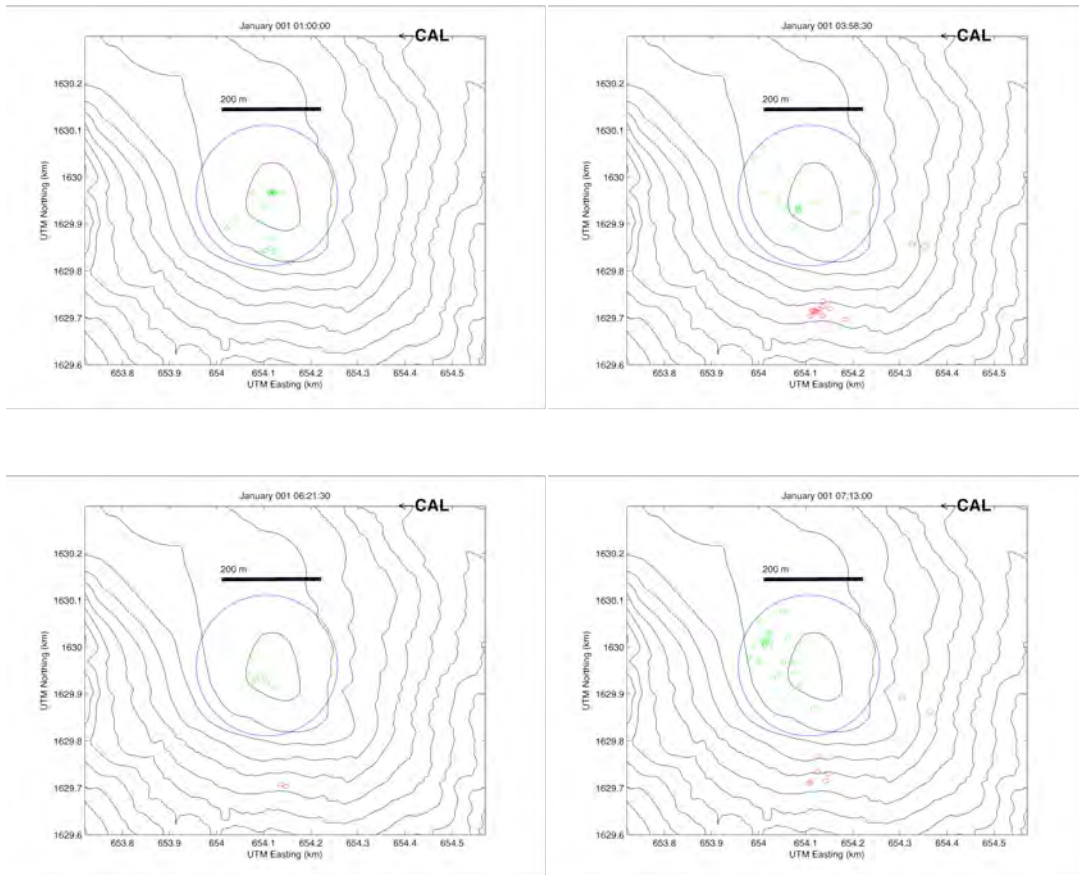
Shishaldin volcano, Alaska: 1. Origin of Strombolian activity, *Journal of Volcanology and Geothermal Research*, 137(1-3), 109-134.

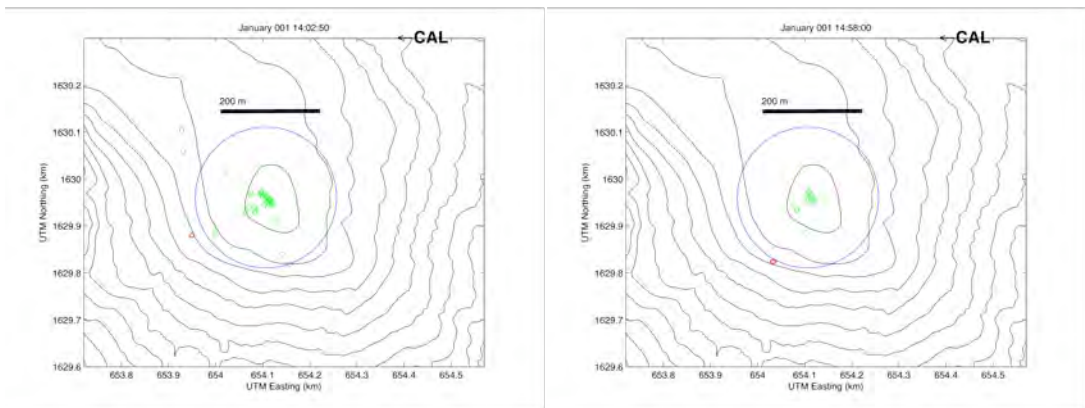
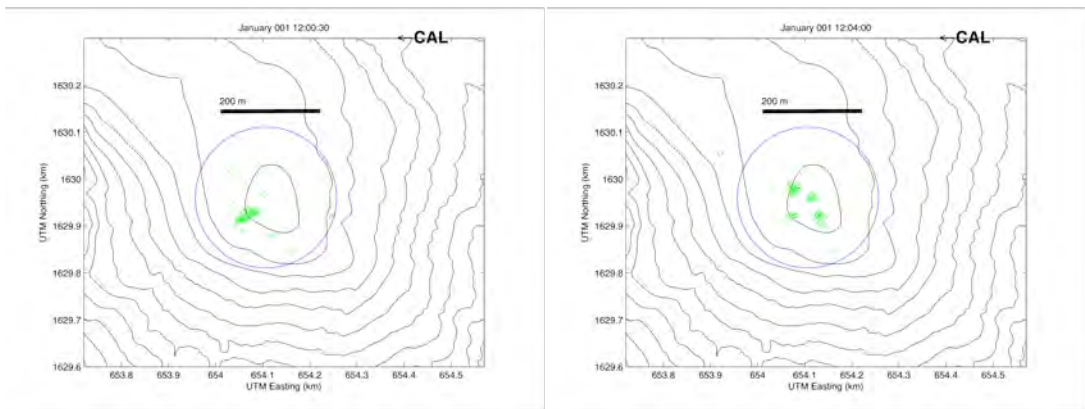
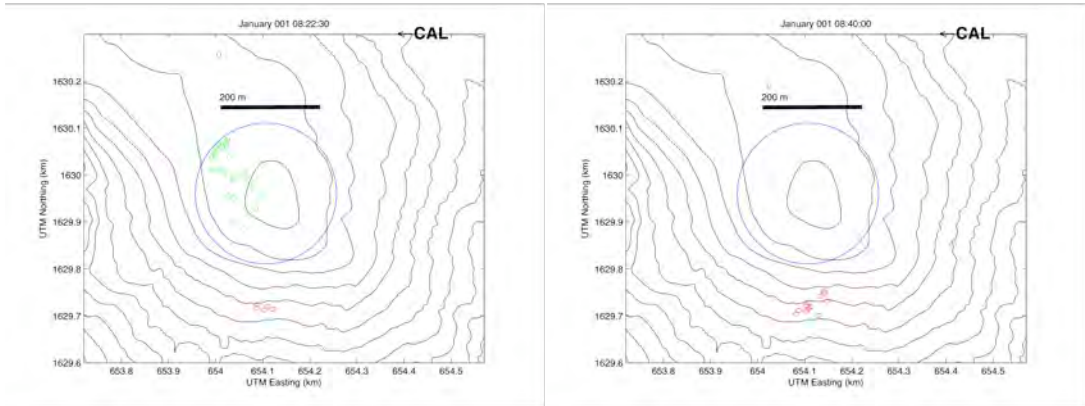
Vergniolle, S., and J. Caplan-Auerbach (2004), Acoustic measurements of the 1999 basaltic eruption of Shishaldin volcano, Alaska: 2. Precursor to the Subplinian phase, *Journal of Volcanology and Geothermal Research*, 137(1-3), 135-151.

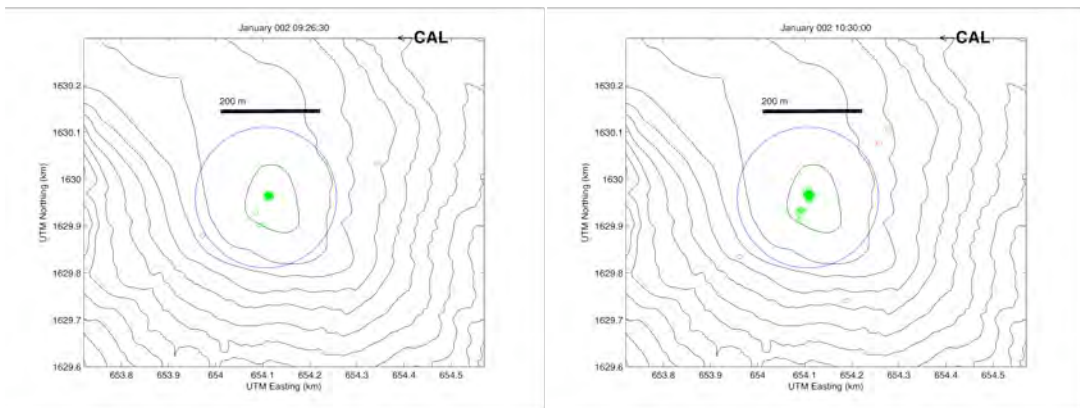
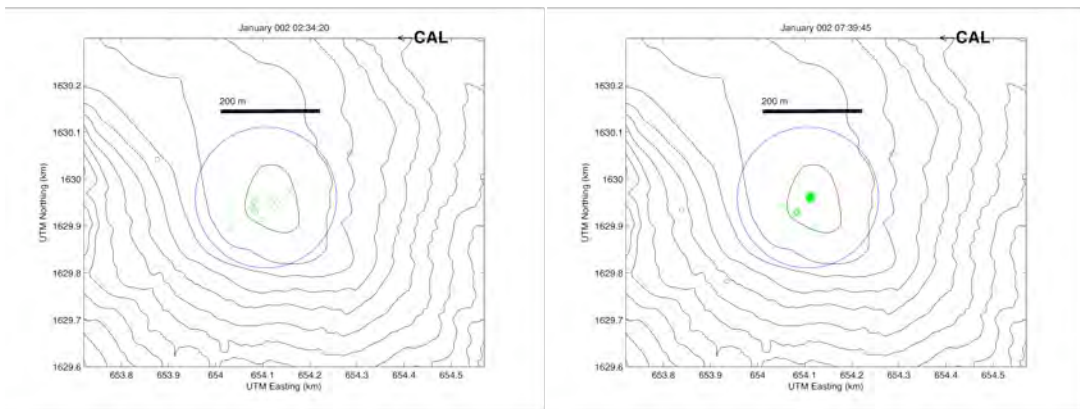
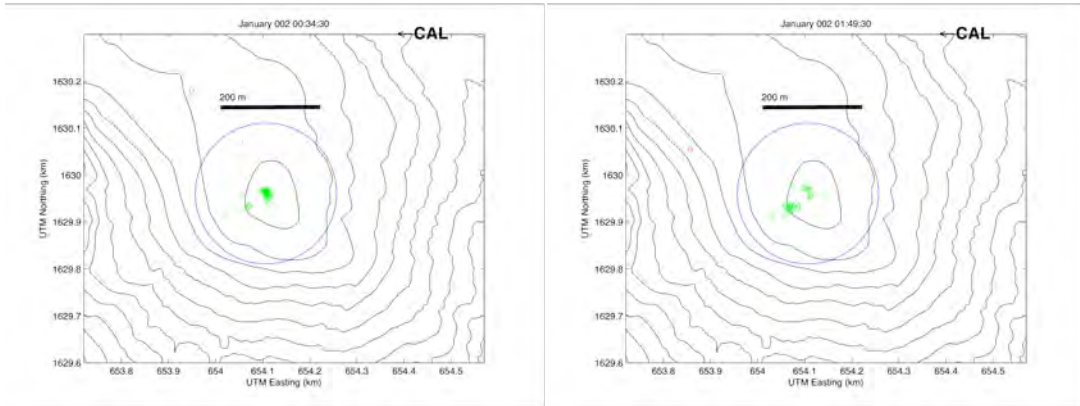
Wilson, C. R., et al. (1966), Evidence of Two Sound Channels in the Polar Atmosphere from Infrasonic Observations of the Eruption of an Alaskan Volcano, *Nature*, 211, 163 - 165.

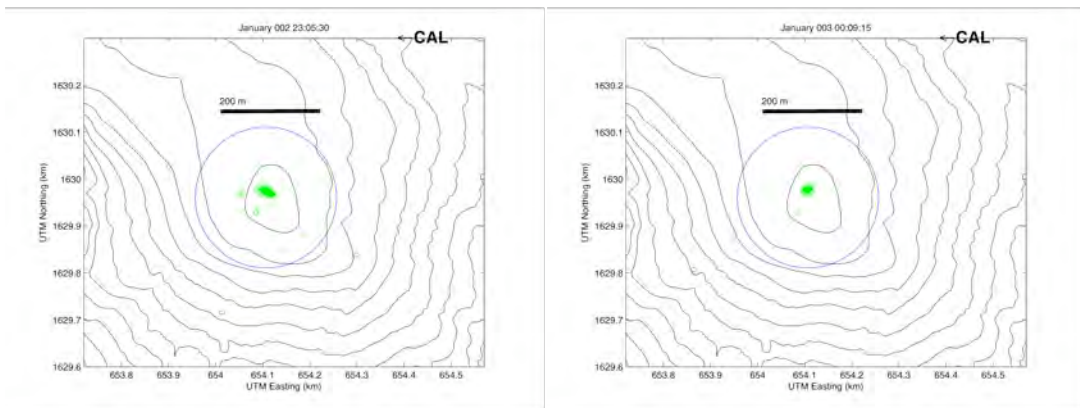
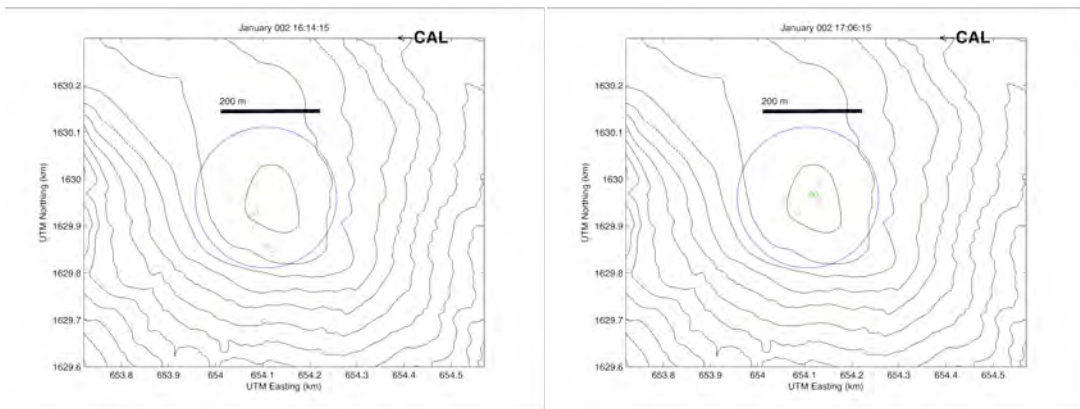
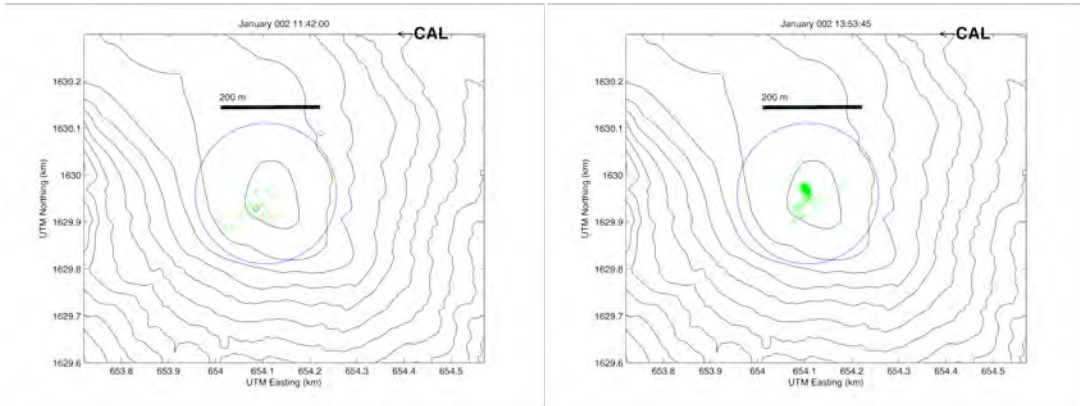
Appendix 1

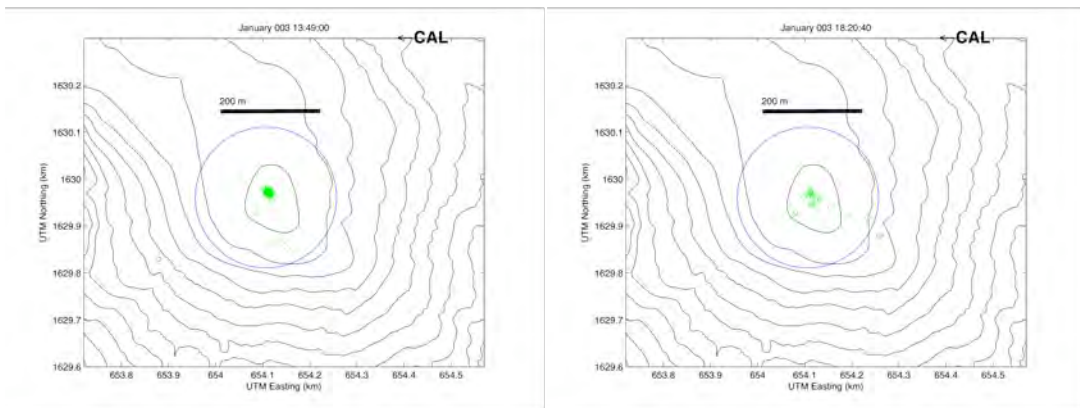
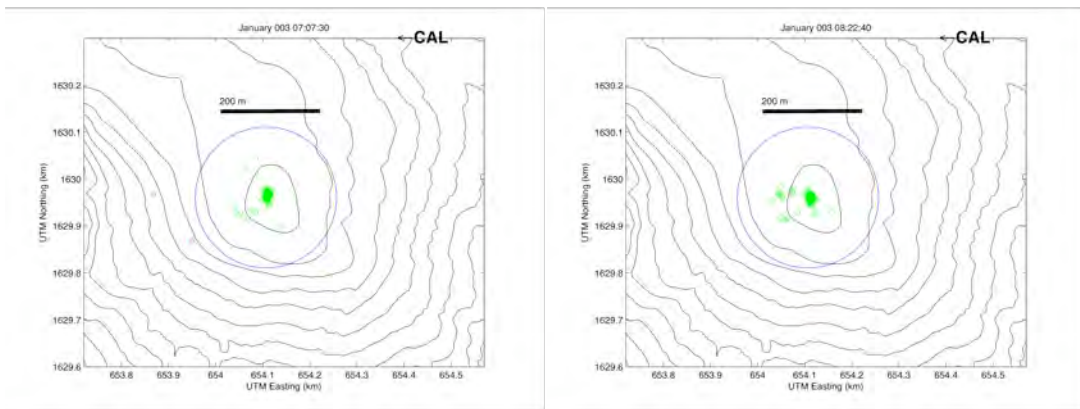
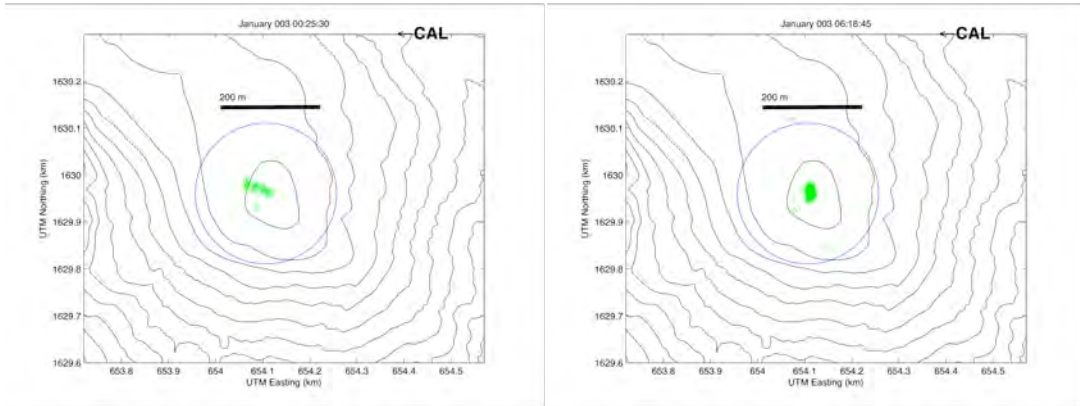
The following figures are sub-event location plots for all long duration events (50 s or longer) from the catalog. The blue circle represents a 300-meter diameter geographical filter where sub-events that are within the filter are plotted in green, and those outside are plotted in red.

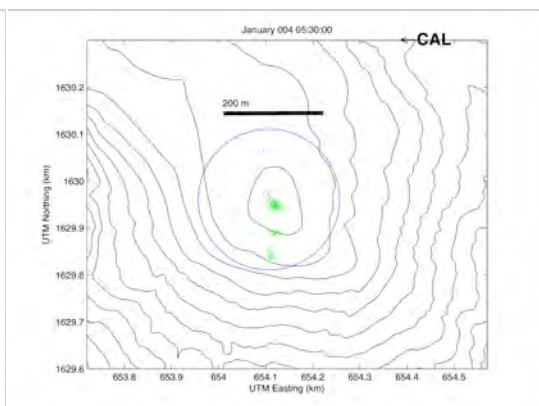
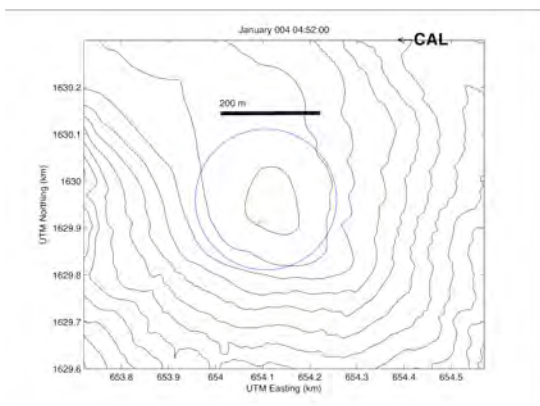
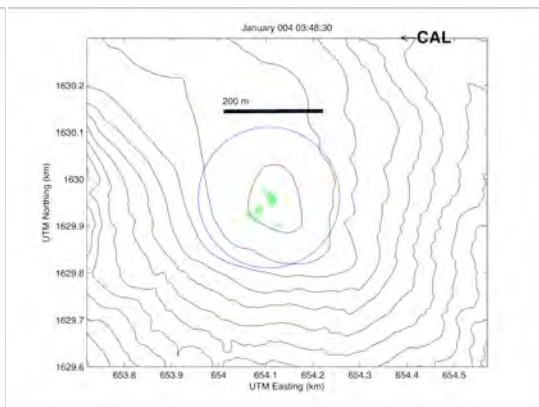
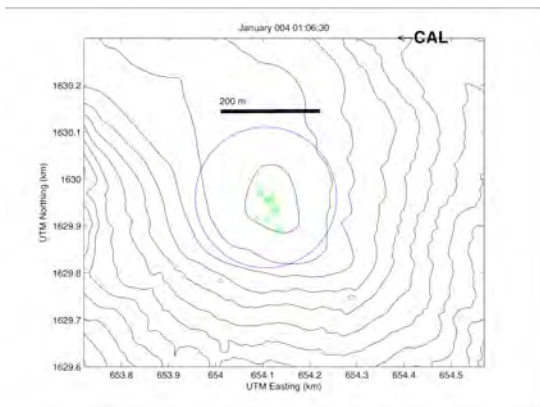
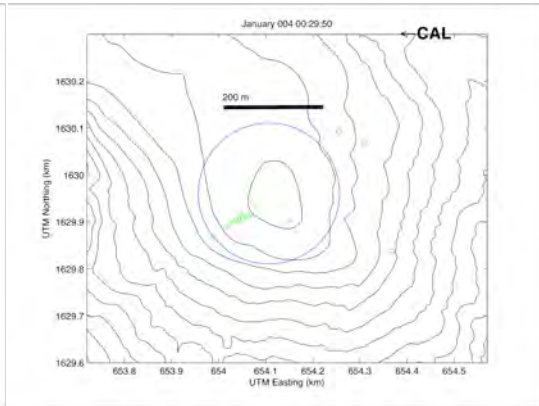
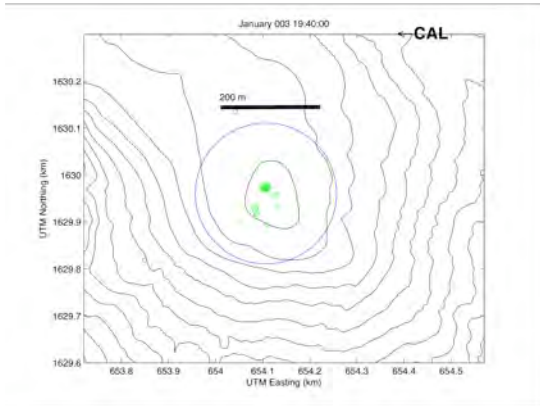


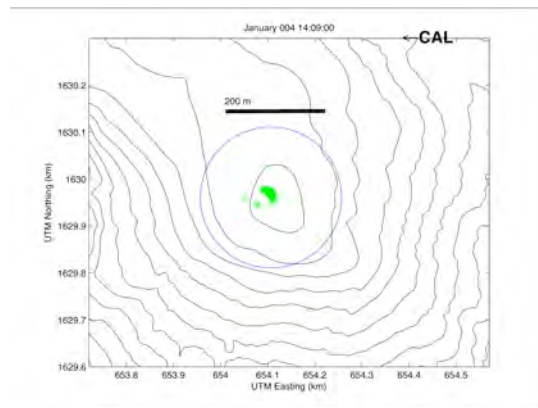
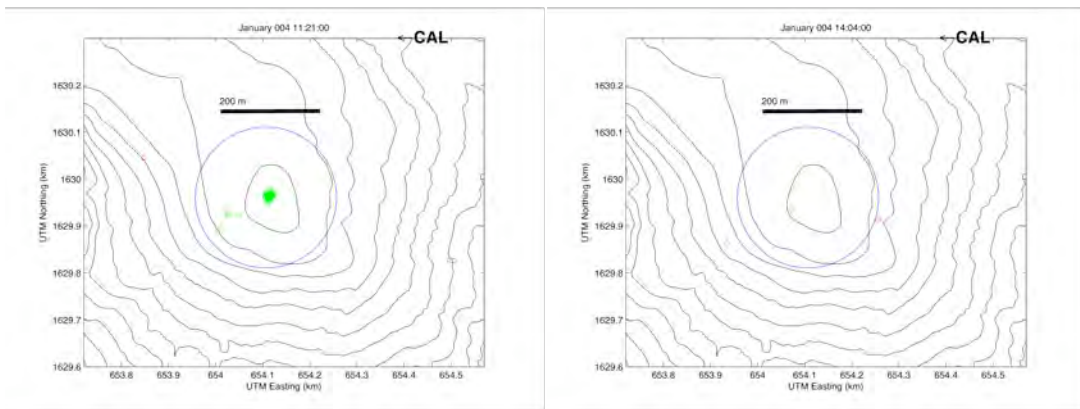
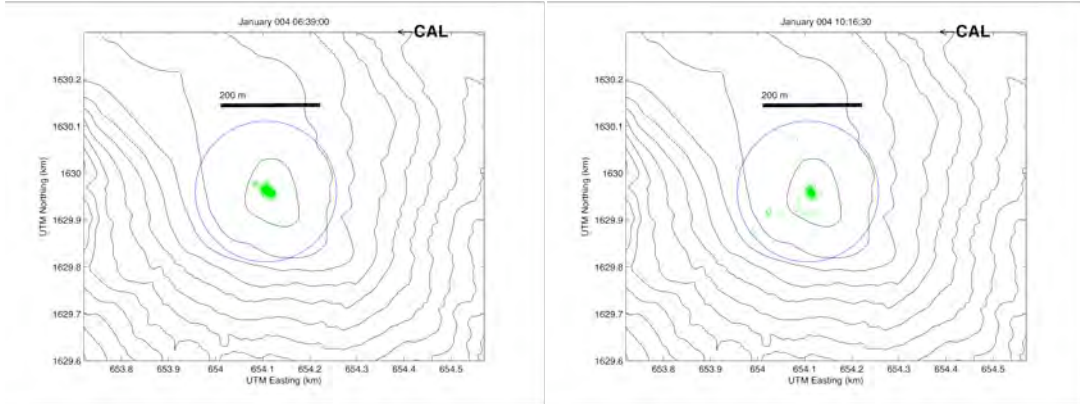




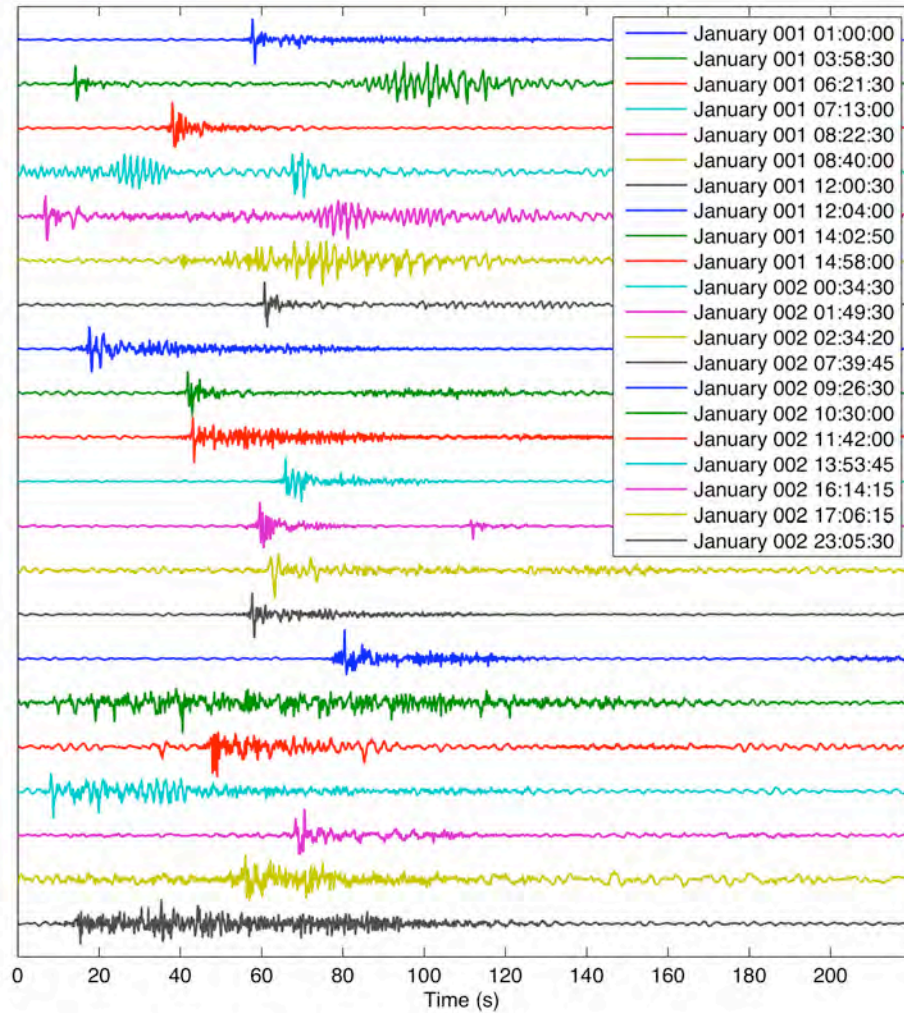


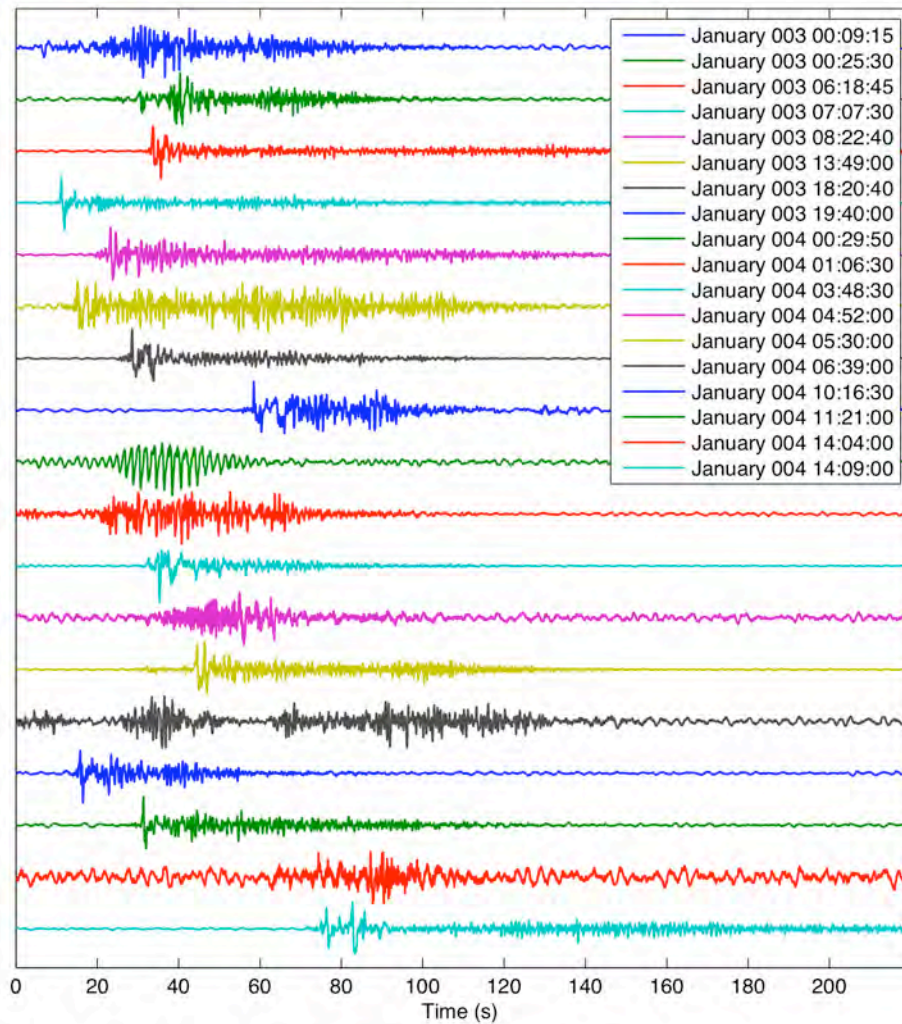




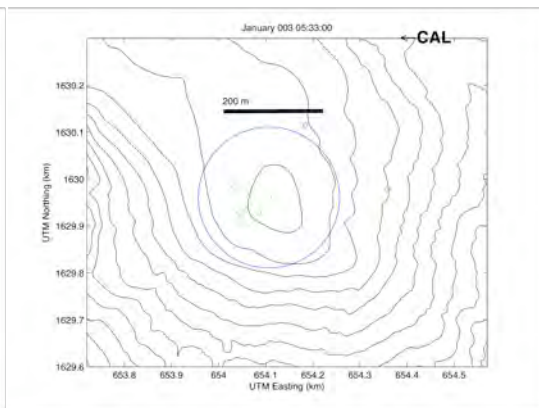
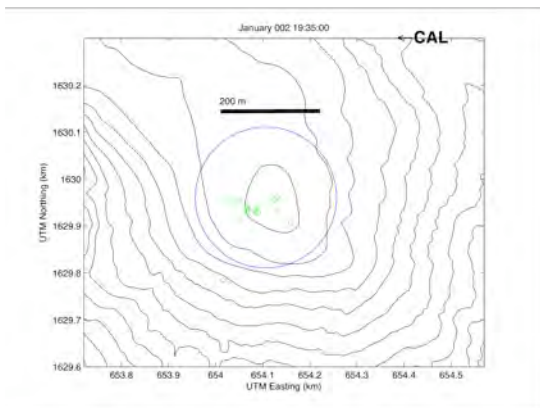
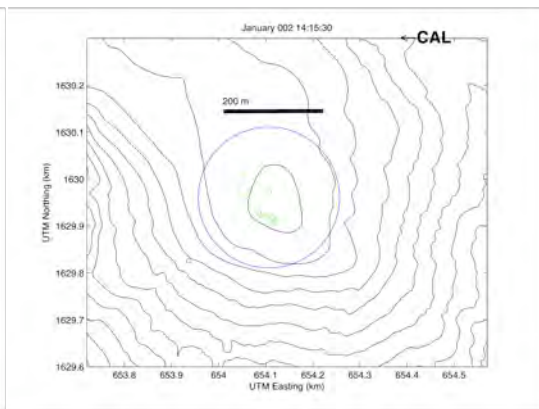
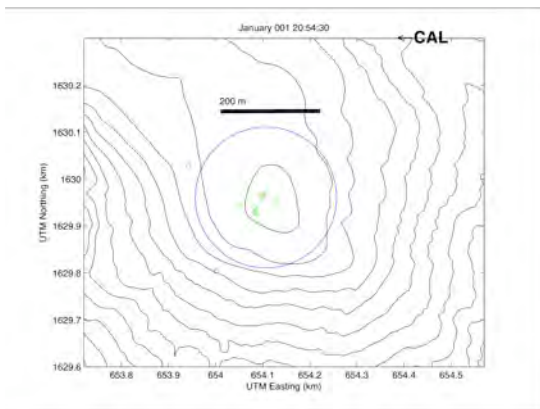
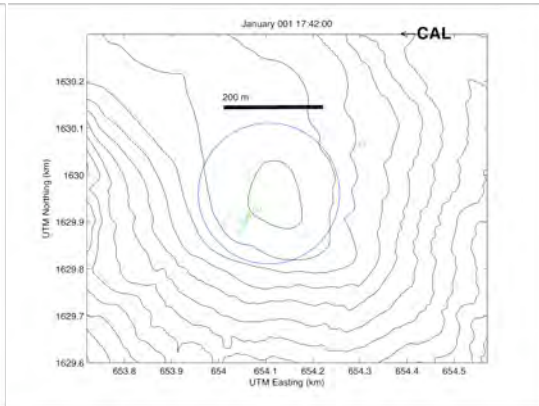
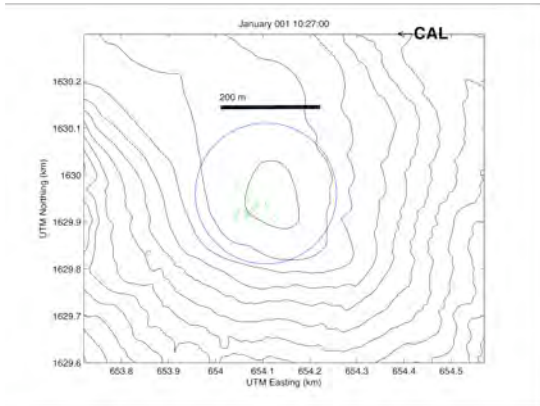


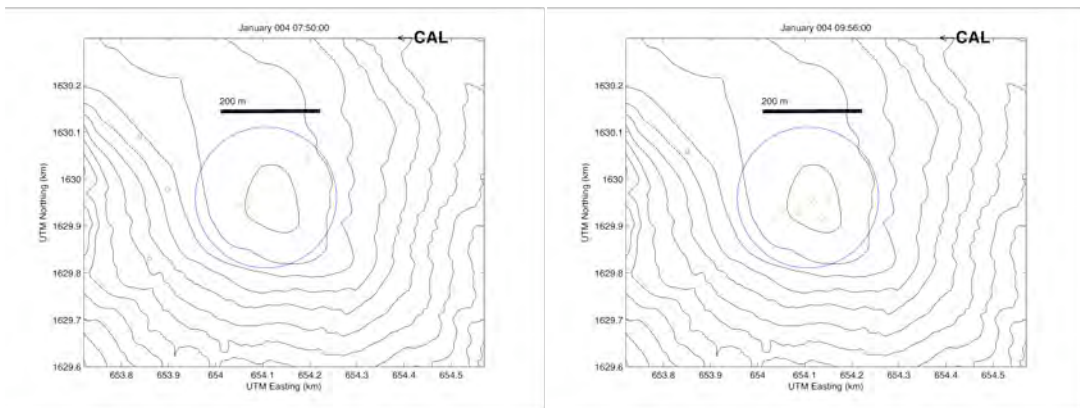
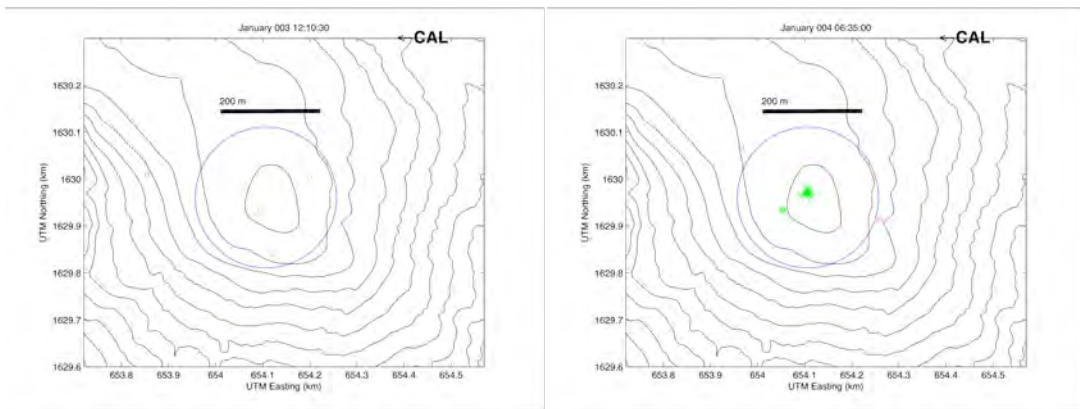
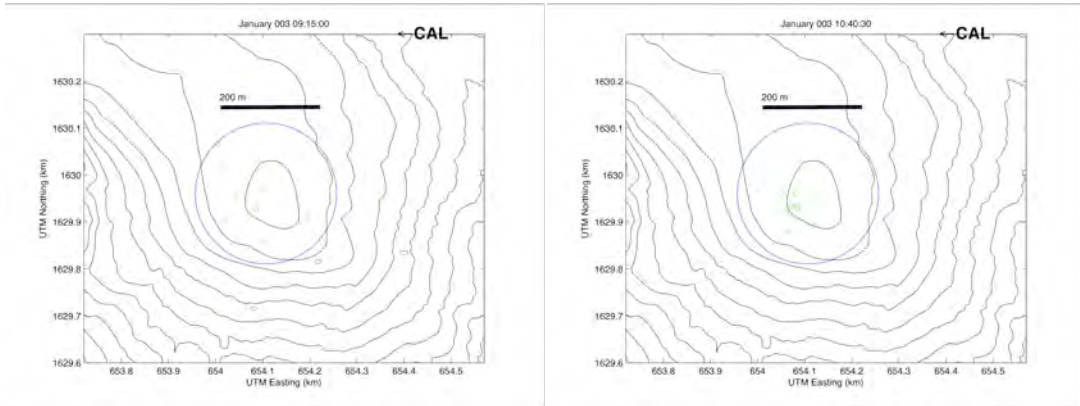
The following two figures are the corresponding waveforms for every long duration (50 s or longer) eruption in the catalog.

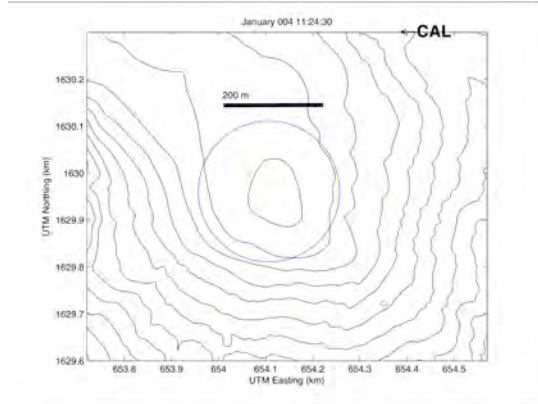




The following figures are sub-event location plots for all short duration events (less than 50 s) from the catalog. The blue circle represents a 300-meter diameter geographical filter where sub-events that are within the filter are plotted in green, and those outside are plotted in red.







The following figure shows the corresponding waveforms for every short duration (less than 50 s) eruption in the catalog.

